A Dual Modular Multilevel Converter With High-Frequency Magnetic Links Between Submodules for MV Open-End Stator Winding Machine Drives

Mohamed S. Diab, Ahmed M. Massoud, *Senior Member, IEEE*, Shehab Ahmed, *Senior Member, IEEE*, and Barry W. Williams

***Abstract*—This paper presents a dual modular multilevel converter (MMC) topology that utilizes energy exchange between adjacent-arm submodules (SMs), operating with out-of-phase modulation. The proposed configuration is applicable to medium-voltage high-power variable-speed drives incorporating open-end stator winding machines. A novel concept of power decoupling between adjacent-arm SMs in the dual MMC topology is realized through high-frequency transformer-based dc–dc converter modules. This concept offers a significant reduction in the sizing requirement of the SM capacitance and the stored energy in the MMC system, while avoiding the problem of wide voltage fluctuations of SM capacitors, especially at low operating frequencies. The proposed configuration can produce dc voltage; therefore, a machine speed range from zero speed to the rated speed is possible under the rated torque operating condition. The operating principles of the proposed dual MMC configuration are elaborated and necessary mathematical analysis is derived. Simulation and experimental results verify the concept of the proposed drive configuration.**

***Index Terms*—Dual half bridge (DHB), high-frequency (HF) transformer, low motor speed, medium-voltage (MV) variable-speed drives, modular multilevel converter (MMC), open-end stator winding machines, submodule (SM) capacitor voltage ripple.**

I. Introduction

INTEREST in the modular multilevel converter (MMC) has been steadily grown due to its promising potential, enabling it to be suitable for medium-voltage (MV) to high-voltage high-power applications such as high-voltage direct-current (HVdc) transmission and MV motor drive applications [1]–[10]. The salient features of the MMC can be summarized in its high modularity, ease of scalability, and enhanced reliability. In addition to its merits, the shortcomings of classical multilevel converter topologies, such as diode-clamped [11], flying-capacitor [12], and cascaded H-bridge converters [13], result in the MMC being the standard commercialized converter interface in the HVdc field, but not yet in MV adjustable-speed drive applications. The main reason is that MMC-fed adjustable-speed drives suffer from power imbalance problems between the upper and lower arms when operating at high-torque and low-speed conditions, where the voltage fluctuations of the MMC floating capacitors are directly proportional to the magnitude of the output current, while inversely proportional to the operating frequency. With this serious challenge, the MMC is not suitable to drive a motor at a constant torque while Volt/Hertz control is applied, which constrains its application in a narrow range of quadratic-torque loads, such as fans, pumps, and compressors [14], [15].

Reviewing the literature, several approaches have been proposed to restrain the inherent problem of wide voltage fluctuations of the MMC floating capacitors at low operating frequencies. The most effective approach to suppress the capacitor voltage ripple is to inject a high-frequency (HF) circulating current into the MMC phase arms, while injecting the same frequency harmonic into the converter output common-mode (CM) voltage [15]–[24]. With this approach, two degrees of freedom are created and can be exploited to redistribute the power between the upper and lower MMC arms, where both injected signals produce an HF power exchange between the arms, allowing the submodule (SM) capacitors to be charged and discharged more frequently such that their voltage ripple is attenuated. In order to reduce the peak of the injected signals, and, hence, to reduce losses, the injected circulating current waveform is reshaped from sinusoidal waveform [16]–[20] into a square waveform [21]–[24] and third-order current harmonic as well [15]. Although this compensation approach limits capacitor voltage variation at low motor speeds, the CM voltage introduced at the motor terminals results in insulation and bearing current

Manuscript received May 9, 2017; accepted July 21, 2017. Date of publication August 2, 2017; date of current version February 22, 2018. Recommended for publication by Associate Editor B. Wang. *(Corresponding author: Mohamed Said Diab.)*

M. S. Diab is with the Department of Electronic and Electrical Engineering, University of Strathclyde, Glasgow G1 1XQ, U.K., and also with the Electrical Engineering Department Faculty of Engineering, Alexandria University, Alexandria 21544, Egypt (e-mail: m.said@spiretronic.com).

A. M. Massoud is with the Department of Electrical Engineering, Qatar University, Doha 2713, Qatar (e-mail: ahmed.massoud@qu.edu.qa).

S. Ahmed is with the Department of Electrical and Computer Engineering, Texas A&M University at Qatar, Doha 23874, Qatar (e-mail: shehab.ahmed@qatar.tamu.edu).

B. W. Williams is with the Department of Electronic and Electrical Engineering, University of Strathclyde, Glasgow G1 1XQ, U.K. (e-mail: barry.williams@strath.ac.uk).

Color versions of one or more of the figures in this paper are available online at http://ieeexplore.ieee.org.

Digital Object Identifier 10.1109/TPEL.2017.2735195

problems that harm the motor and shorten its lifetime. Also, the high magnitude of the HF arm currents significantly increases current stress, and, consequently, power loss, which necessitates oversizing the current rating of the switching devices. In addition, a conflict in coordinating the control of the intentionally injected signals and the basic MMC control loops may arise, causing stability problems during transient conditions.

Revisiting other approaches that address MMC low-frequency operation through the proposal of new control methods, operation modes, or modulation techniques; an approach which applies a flexible control scheme for MMC capacitor voltage as a motor drive was proposed in [25] and [26]. In this approach, the SM capacitor voltage can be varied in accordance to the motor speed by regulating both the dc and ac components of the pulse-width modulation (PWM) reference signal, which allows increasing capacitor voltage ripple as the motor speed decreases without exceeding the maximum peak capacitor voltage. Asymmetric MMC operation mode, to avoid dc-link voltage influence on the capacitor ripple, was presented in [27]. By forcing one arm to apply the major dc-link voltage while renouncing the contribution in output current generation, the other arm sustains almost all output current with a low dc-link voltage. The quasi two-level MMC operation, proposed in [28], has been extended to a triangle-carrier-based PWM technique in order to synthesize low-frequency output waveforms as in the conventional two-level PWM voltage-source inverter, which reduces arm energy variations [29].

On the other hand, various modifications to the basic MMC structure have been adopted in an attempt to find a hardware solution to tightly control capacitor voltage ripple at low-frequency operation of adjustable-speed drives. A power transfer channel has been introduced to provide power balance between the upper and lower MMC arm by a cross connection of the middle taps of both arms through an additional path of either series-connected half-bridge SMs (HB-SMs) [30] or a flying capacitor [31], for each MMC phase leg. In both schemes, an HF voltage is introduced into the subarms, which excites an HF current in the additional cross-connected path to create one degree of freedom for power redistribution between both the upper and lower arms. Other configurations addressed MMC low-frequency operation by employing full-bridge SMs instead of the HB-SMs [32], suggesting an MMC-based hexverter topology for energy-balance control [33], combining the conventional MMC configuration with a series switch to the dc input source to reduce the average dc components in the arm voltages by disconnection of the dc source at regular intervals [34], and connecting the capacitors of the top SMs and the bottom SMs via two accessorial cables, while connecting the upper and lower arms through a central SM [35].

Nonetheless, all of the abovementioned approaches are unable to drive a machine at full-load and zero-speed conditions. Also, most studies address low-frequency operation of MMC-fed variable-speed drives as a transient condition during starting instead of considering it as a continuous operating mode. Moreover, no further detailed verification and results have been presented for high-power machines with multimegawatt drive systems.

To provide a reliable solution that overcomes the discussed limitations of MMC-fed variable-speed drives, this paper proposes a dual MMC configuration for MV high-power variable-speed drives incorporating an open-end stator winding machine. The concept of the proposed configuration is inspired by the adverse coupling and interaction between arm stored energies. For instance, if the upper arm needs to charge energy, the lower arm needs to discharge the same amount of energy. That is, the proposed configuration allows a bidirectional energy exchange between each pair of adjacent arms of the dual MMC, operating with out-of-phase modulation, through modular isolated dc–dc converters interfacing each front-to-front SM. With bidirectional energy exchange between oppositely modulated adjacent-arm SMs, the capacitive energy is evenly redistributed among adjacent arms in the same dual leg, eliminating the wide variation of capacitor voltage ripple, independent of the operating frequency. This allows the MMC to drive a variable-speed machine at constant torque over the whole speed range, even at standstill condition. Although the proposed configuration adds hardware to the basic MMC structure, it significantly reduces the SM capacitance, and, hence, the energy stored in the MMC system. Furthermore, the control of the added energy-exchange modules is independent of the main MMC system control loops.

The outline of this paper is as follows. Section II addresses the operating principles of the dual MMC topology for open-end stator winding machines. The proposed dual MMC configuration, with energy exchange dc–dc converter modules, is illustrated in Section III. Simulation results for multimegawatt MMC systems are presented in Section IV, while experimental results for a scaled-down laboratory prototype are presented in Section V. Assessment of the proposed MMC configuration is discussed in Section VI. Finally, Section VII concludes the contributions of this paper.

II. Dual MMC Topology for Open-End Stator Winding Machines

Machines with open-end stator windings are a possible alternative to conventional star- and delta-connected stators, that not only suppress switching CM voltages but also improve output voltage quality [36]–[40]. The concept of employing a dual-inverter configuration feeding each end of an open-end stator winding induction motor was first introduced in [41] for MV high-power applications. The topology has been implemented using two two-level inverters, while it is capable of generating three-level output voltage with half the dc-link voltage compared to a single-sided three-level inverter topology. Similarly, a dual three-level inverter configuration with a single dc-link voltage was proposed for five-level operation [42]. Thereafter, several multilevel topologies have been considered for open-end stator winding machines with various topologies [39], [43]–[45]. Recently, a dual-inverter configuration based on the MMC has been proposed with many advantages [46], where it offers single dc-source operation regardless of the number of output voltage levels, which eliminates bulky and expensive multiwinding isolation transformers to provide isolated dc sources. Also, the dual MMC configuration achieves the same maximum output voltage

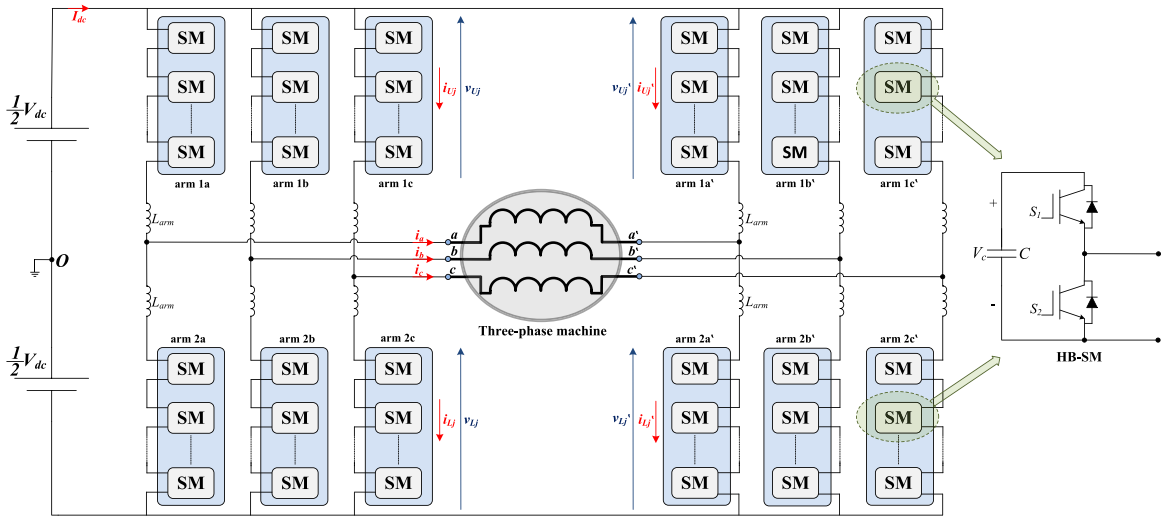

Fig. 1. Circuit configuration of a three-phase dual-MMC-fed open-end stator winding machine.

magnitude as the conventional single-sided MMC with half of the dc-link voltage, which reduces the insulation requirement. If one converter fails, the other converter can continue operation with a reduced output power while reconfiguring the machine end terminals at the faulty converter side to be connected in star or delta, which gives the dual configuration an intrinsic fault-tolerant capability. Moreover, it offers higher redundant switching state combinations, compared to a single-sided MMC with the same number of output voltage levels, that can be exploited in voltage balancing of the floating capacitors.

The circuit diagram of a three-phase dual MMC configuration is shown in Fig. 1, where it consists of an MMC feeding each end of the machine stator windings, while both MMCs operate in an out-of-phase manner. Each MMC is composed of three-phase legs, each formed by two arms connected in series through arm inductors L_{arm}. Each arm consists of N series-connected SMs, while the SM commonly consists of an HB cell with a dc capacitor of an equivalent capacitance C and a rated voltage V_c. Although the number of arm inductors is doubled compared to a conventional single-sided MMC topology, the equivalent arm inductance of the dual MMC topology remains the same. The dual MMC structure can be considered as a direct consequence of splitting each phase leg of a conventional single-sided MMC into dual complemented legs each with half the number of SMs, compared to the single-sided phase leg. Thus, for the same amount of power, the total number of SMs employed in a dual MMC configuration is same as the number of SMs in a conventional single-sided topology. Additionally, the voltage and current stress of the SM capacitors and switching devices is identical in both MMC configurations.

A. Basic Circuit Analysis

Referring to Fig. 1, the terminals of the open-end machine windings connected to the left-side MMC are denoted by a, b, c, while a', b', c' will represent the terminal ends connected to the right-side MMC. The voltage across each phase winding is the differential voltage between both machine winding terminals, and is denoted by $v_{jj'}$, while the current through the machine winding is denoted by i_j, where $j \in \{a,\ b,\ c\}$, and are given as follows:

$$v_{jj'} = V_o \cos(\omega t + \theta_j) \tag{1a}$$

$$i_j = I_o \cos(\omega t + \theta_j - \emptyset) \tag{1b}$$

where ω is the output angular frequency, θ_j is the phase angle of the stator voltage ($\theta_a = 0°,\ \theta_b = 120°,$ and $\theta_c = 240°$), and $\emptyset$ is the machine power-factor angle. V_o and I_o are the magnitudes of the voltage across the machine windings and their current's, respectively. The magnitude of the ac output voltage is bounded by the modulation index M and the voltage of the input source V_{dc}, as in (2). It is worth noting that the utilization of the dc-link voltage is doubled with the dual-converter configurations, compared to a single-sided topology

$$V_o = MV_{\text{dc}}. \tag{2}$$

Since each two MMC legs with a common machine winding have an out-of-phase modulation, the reference voltages for MMC arms, in both converter side, in addition to the arm currents are given by (3) and (4), respectively, with the subscripts U and L referring to the corresponding "upper" and "lower" arm

$$v_{Uj} = v_{Lj'} = \frac{1}{2}V_{\text{dc}} - \frac{1}{2}v_{jj'} \tag{3a}$$

$$v_{Lj} = v_{Uj'} = \frac{1}{2}V_{\text{dc}} + \frac{1}{2}v_{jj'} \tag{3b}$$

$$i_{Uj} = i_{\text{cm}\,j} + \frac{1}{2}i_j \tag{4a}$$

$$i_{Lj} = i_{\text{cm}\,j} - \frac{1}{2}i_j \tag{4b}$$

$$i_{Uj'} = i_{\text{cm}\,j'} - \frac{1}{2}i_j \tag{4c}$$

$$i_{Lj'} = i_{\text{cm}\,j'} + \frac{1}{2}i_j \tag{4d}$$

where $i_{\text{cm } j}$ and $i_{\text{cm } j'}$ are the CM currents of each two complemented legs in the dual MMC topology, and often referred to as circulating currents. Ideally, these CM currents should be equal to a constant dc component which depends on the number of MMC phase legs and the active power delivered from or to the dc link. However, the mutual interaction between the arm inductors and the SM capacitors induces a series of even-order harmonics that appear in an out-of-phase profile in both CM currents [47]. With appropriate even-order harmonic suppression control [48], [49], both CM currents can be considered as only a dc component which can be calculated for a dual three-phase MMC through a lossless power balance between the dc input and ac output as shown in (5), with I_{dc} is the dc input current of the dual MMC

$$i_{\text{cm } j} = i_{\text{cm } j'} = \frac{I_{\text{dc}}}{6} = \frac{M I_o \cos \emptyset}{4}. \tag{5}$$

B. Energy Variation Analysis

In this section, the analysis of energy variation is conducted for a general phase-leg *j* of the left-side MMC. The same analysis applies to the other phase legs, denoted by j' of the right-side MMC, however, in an out-of-phase manner. The instantaneous power of each arm is given by the product of the arm voltage (3) and the corresponding arm current (4):

$$p_{Uj} = v_{Uj}\, i_{Uj} \tag{6a}$$

$$p_{Lj} = v_{Lj}\, i_{Lj}. \tag{6b}$$

Substituting (1)–(5) into (6) yields

$$p_{Uj} = \frac{V_{\text{dc}}\, I_o}{4} \left[\cos(\omega t + \theta_j - \emptyset) - \frac{M^2}{2} \cos(\emptyset) \cos(\omega t + \theta_j) - \frac{M}{2} \cos[2(\omega t + \theta_j) - \emptyset] \right] \tag{7a}$$

$$p_{Lj} = \frac{V_{\text{dc}}\, I_o}{4} \left[-\cos(\omega t + \theta_j - \emptyset) + \frac{M^2}{2} \cos(\emptyset) \cos(\omega t + \theta_j) - \frac{M}{2} \cos[2(\omega t + \theta_j) - \emptyset] \right]. \tag{7b}$$

The instantaneous power in the upper and lower arms can be categorized into a CM component p_{cm}, which is in phase in both arms, and a differential-mode (DM) component p_{dm}, which is in antiphase in the upper and lower arms. The CM component alternates at twice the line frequency, and is a direct consequence of the active power at the dc side being constant, whereas the phase power at the ac side pulsates at twice the line frequency. The DM component alternates with the fundamental line frequency, and represents the power which is circulated back and forth internally between the upper and lower arms of the same leg. Accordingly

$$p_{\text{cm}} = -\frac{V_{\text{dc}}\, I_o M}{8} \cos[2(\omega t + \theta_j) - \emptyset] \tag{8a}$$

$$p_{\text{dm}} = \frac{V_{\text{dc}}\, I_o}{4} \left[\cos(\omega t + \theta_j - \emptyset) - \frac{M^2}{2} \cos(\emptyset) \cos(\omega t + \theta_j) \right] = \frac{V_{\text{dc}}\, I_o}{8} \sqrt{4 + \cos^2(\emptyset)\,(M^4 - 4M^2)} \cos(\omega t + \theta_j - \gamma) \tag{8b}$$

$$\gamma = \emptyset + \tan^{-1} \frac{M^2 \tan \emptyset \cos^2 \emptyset}{2 - M^2 \cos^2 \emptyset}. \tag{9}$$

Similar to the instantaneous power, the energy variation of the arms can be classified into a CM component w_{cm} and a DM component w_{dm} given by

$$w_{Uj} = w_{\text{cm}} + w_{\text{dm}} \tag{10a}$$

$$w_{Lj} = w_{\text{cm}} - w_{\text{dm}} \tag{10b}$$

where w_{Uj} and w_{Lj} are the alternating components of the stored energy in the upper and lower arms, respectively. Integrating (8) yields both CM and DM components of the energy variation as follows:

$$w_{\text{cm}} = -\frac{V_{\text{dc}}\, I_o M}{16\omega} \sin[2(\omega t + \theta_j) - \emptyset] \tag{11a}$$

$$w_{\text{dm}} = \frac{V_{\text{dc}}\, I_o}{8\omega} \sqrt{4 + \cos^2(\emptyset)\,(M^4 - 4M^2)} \sin(\omega t + \theta_j - \gamma). \tag{11b}$$

C. Capacitor Voltage Analysis

Due to the dual-frequency alternation of the capacitive energy stored in the MMC arms, capacitor voltage fluctuations have both CM and DM voltage-ripple components alternating at twice the fundamental frequency and at the fundamental frequency, respectively, shown by

$$\Delta v_{cUj} = -\frac{\Delta V_{c_{\text{cm}}}}{2} \sin[2(\omega t + \theta_j) - \emptyset] + \frac{\Delta V_{c_{\text{dm}}}}{2} \sin(\omega t + \theta_j - \gamma) \tag{12a}$$

$$\Delta v_{cLj} = -\frac{\Delta V_{c_{\text{cm}}}}{2} \sin[2(\omega t + \theta_j) - \emptyset] - \frac{\Delta V_{c_{\text{dm}}}}{2} \sin(\omega t + \theta_j - \gamma) \tag{12b}$$

where Δv_{cUj} and Δv_{cLj} are the capacitor voltage variation of SMs in the upper and lower arms of the left-side MMC, respectively, while $\Delta V_{c_{\text{cm}}}$ and $\Delta V_{c_{\text{dm}}}$ are the absolute values of the peak-to-peak variation of the CM and DM components of SM capacitor voltage ripple. That is, the variation of the arm stored energy is handled by the capacitors of the series-connected SMs in each arm as demonstrated by

$$\Delta W = \frac{NC}{2} \left(V^2{}_{c\ \max} - V^2{}_{c\ \min} \right) = NCV_c\, \Delta V_c \tag{13}$$

where ΔW and ΔV_c are the peak-to-peak variation of the arm stored energy and capacitor voltage ripple of each SM, respectively. Since the average voltage across each SM capacitor is $V_c = V_{\text{dc}}/N$, then the magnitude of the peak-to-peak capacitor voltage ripple due to CM and DM components, from (11)

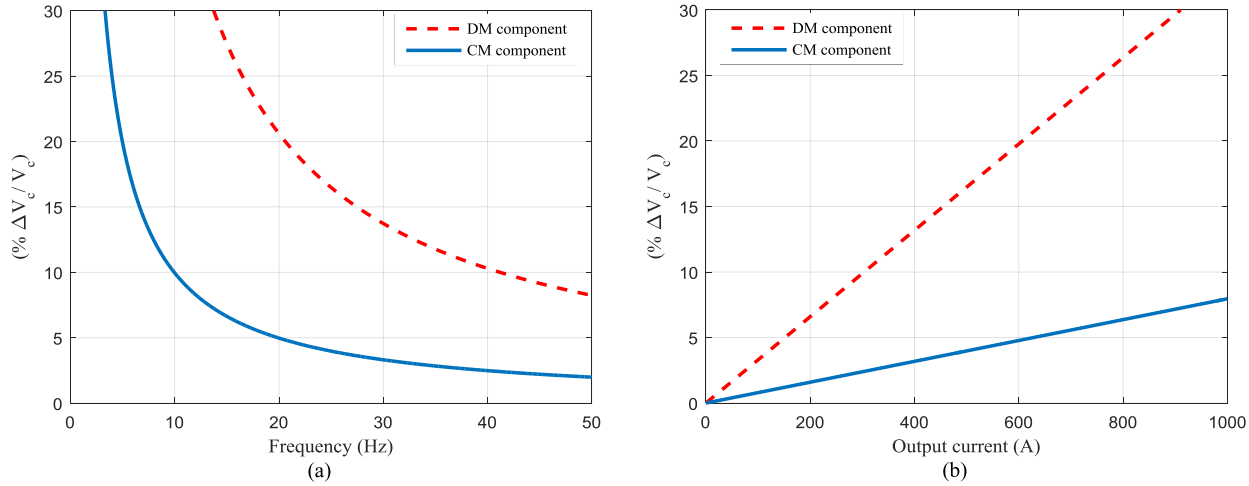

Fig. 2. Normalized components of capacitor voltage ripple, with $V_c = 2.5$ kV, $C = 3$ mF, $M = 0.75$, and $\emptyset = 25°$ at (a) variable frequency and constant output current ($I_o = 500$ A) and (b) variable output current and constant frequency ($f = 25$ Hz).

and (13) are

$$\Delta V_{c_{\text{cm}}} = \frac{I_o M}{8\omega C} \tag{14a}$$

$$\Delta V_{c_{\text{dm}}} = \frac{I_o}{4\omega C}\sqrt{4 + \cos^2(\emptyset)\,(M^4 - 4M^2)}. \tag{14b}$$

The CM component of the capacitor voltage ripple is a direct result of the CM power given by (8a), which is inherited in the converter due to the different frequency of the input and output powers. Although this CM component is inevitable, it has a slight influence on the capacitor voltage ripple as demonstrated by (14a), where in variable-speed drives with Volt/Hertz control, the ratio M/ω is near constant, while the load current I_o is invariant. On the other side, when the operating frequency ω is reduced in (14b), while the ratio M/ω is constant for constant motor torque requirements, the DM component of the capacitor voltage ripple increases. Furthermore, the direct proportionality of capacitor voltage ripple to output current variation, at a constant operating frequency, is much higher in the DM component compared to the CM component. The significant influence of the DM component in the capacitor voltage ripple can be emphasized as in Fig. 2, where the normalized peak-to-peak capacitor voltage variation, for both CM and DM components, is illustrated with operating frequency variation in Fig. 2(a) and with output current variation in Fig. 2(b).

Further assessment of both capacitor voltage-ripple components is elucidated in Fig. 3, where the variation of the normalized capacitor voltage ripple for both components is shown with operating frequency variation at different output currents, while the ratio M/ω is constant as required by the Volt/Hertz control. The CM component of the capacitor voltage ripple exhibits a horizontal-line ripple profile with a low magnitude, which is not affected by the operating frequency variation. Also, the ripple profile of the CM component is slightly affected by a corresponding increase in the output current from 200 to 1000 A. In contrast, the ripple profile of the capacitor voltage DM component is significantly increasing at low operating

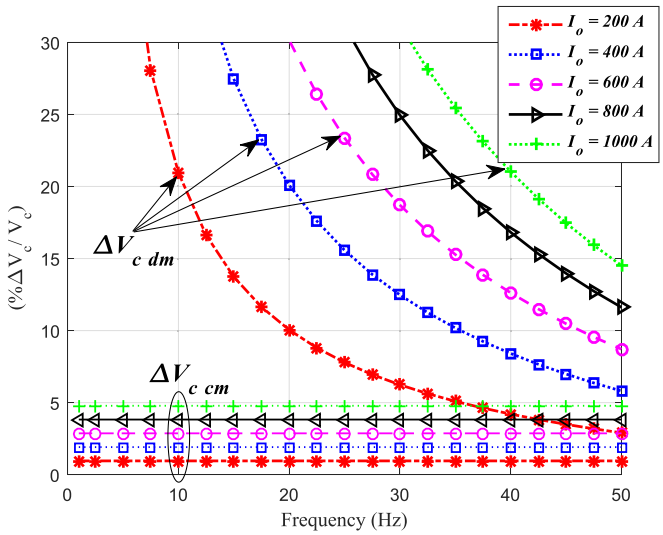

Fig. 3. Normalized components of capacitor voltage ripple at constant M/ω ($C = 3$ mF, $V_c = 2.5$ kV, and $\emptyset = 25°$).

frequencies, while approaching infinity at near-zero frequency. In addition, the DM voltage ripple is much increased as the output current increases. The conclusion is that the dominant component of capacitor voltage ripple is the DM one, which should be tightly controlled so that the capacitor voltage ripple does not exceed tolerated values.

III. Proposed Dual MMC Configuration With Energy-Exchange Modules

The dual MMC topology, illustrated in Section II, implies each machine phase winding be connected differentially between two MMC legs modulated out-of-phase. This out-of-phase modulation associated with a common machine winding keeps the DM component of the energy stored in one MMC arm to alternate with an opposite phase to the same energy component stored in the adjacent arm of the complemented leg.

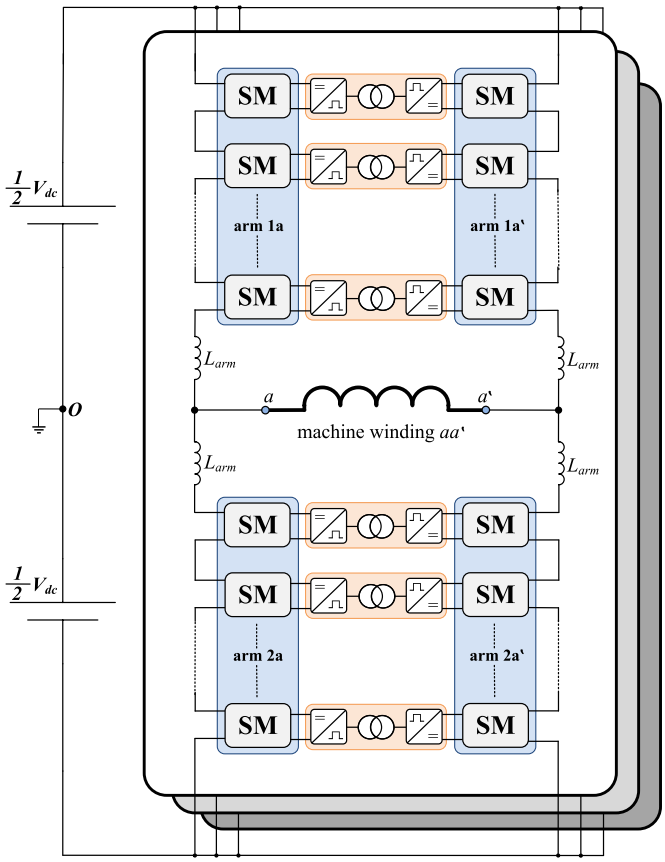

Fig. 4. Circuit diagram for the proposed dual MMC configuration with energy-exchange modules between front-to-front SMs.

Therefore, a proposed scheme to eliminate the DM component in MMC arms is to create a bidirectional energy exchange path between opposite arms in the same dual leg. Since the energy stored in each MMC arm is equally shared by all SMs subsisted by this arm through an individual capacitor voltage-balancing technique, a modular implementation of energy exchange between opposite arms in each dual leg can be achieved by inserting HF transformer-based dc–dc converter modules between front-to-front SMs in the same dual leg. This allows a redistribution of the stored capacitive energy among each front-to-front SM by transferring the DM power component from the SM with arm current charging its capacitor into the adjacent SM with a discharging current direction. With such bidirectional energy transfer between adjacent-arm SMs, the DM component of energy variation can be cancelled, while the CM component is evenly distributed. This approach is illustrated in Fig. 4, where, for brevity, one phase leg of the proposed three-phase dual MMC topology is shown.

A. Isolated Bidirectional DC–DC Converter Modules

The concept of dc–dc conversion via an HF transformer, proposed in [50], can achieve high power density dc–dc conversion with bidirectional power flow, galvanic isolation, high efficiency, low weight and size, and soft semiconductor switching. The phase-shift dual-active-bridge converter is the common implementation of the HF transformer-based dc–dc

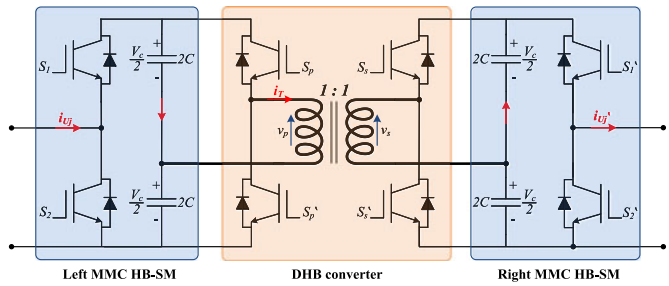

Fig. 5. DHB configuration for front-to-front HB-SMs of the dual MMC topology.

converter, in which two active bridges are interfaced through an HF transformer, where the bridges are phase-shifted relative to each other to control the power transferred from one dc voltage bus to the other. Two configurations among the phase-shift dual-bridge dc–dc converters are the phase-shift dual full-bridge (DFB) and dual half-bridge (DHB) converters [50]–[53]. In a comparison, the DHB topology has half the switching devices and corresponding drivers for the same power rating resulting in an efficient power transfer. In addition, the transformer flux swing of the DHB is only half of DFB's when the same switching frequency and effective cross-sectional area of the transformer core are employed. Therefore, the phase-shift DHB is employed as a dc–dc energy-exchange module for the proposed dual MMC configuration. A detailed circuit diagram for front-to-front SMs in the proposed dual MMC configuration shown in Fig. 4 is elucidated in Fig. 5, where two MMC HB-SMs are interfaced through a DHB converter. The DHB converter consists of two voltage-source HB dc–ac inverters that are coupled to an HF isolation transformer. The turns ratio of the transformer is 1:1 since the dc–dc conversion is only employed for energy exchange between bridge sides at the same voltage level which is equal to the average voltage of the MMC's SM capacitors. The leakage inductance of the transformer is utilized as an interface and energy-transfer element between both voltage-source HB inverters, while the output capacitance of the switching devices is used to realize soft-switching operation [54]. Both HB inverters generate fixed-frequency square-wave voltages with a constant duty ratio of 50%, applied to both transformer sides. The DHB configuration necessitates the capacitor of each MMC SM be equally split with access to the center-tap point as shown in Fig. 5.

The phase-shift angle σ of the two square-wave voltages of the DHB converter determines the amount of power transferred from the leading bridge to the lagging one. With unity transformer turns ratio and equal voltage levels V_c at both bridge sides, the DHB power is expressed as [53]:

$$P = \frac{{V_c}^2 \sigma \left(\pi - |\sigma|\right)}{8\pi^2 f_h L} \tag{15}$$

where L is the transformer leakage inductance and f_h is the DHB switching frequency.

Referring to Fig. 5, the front-to-front MMC SMs are assumed in the upper arms of a general dual leg jj', where a positive half cycle of the output current charges the capacitor of a

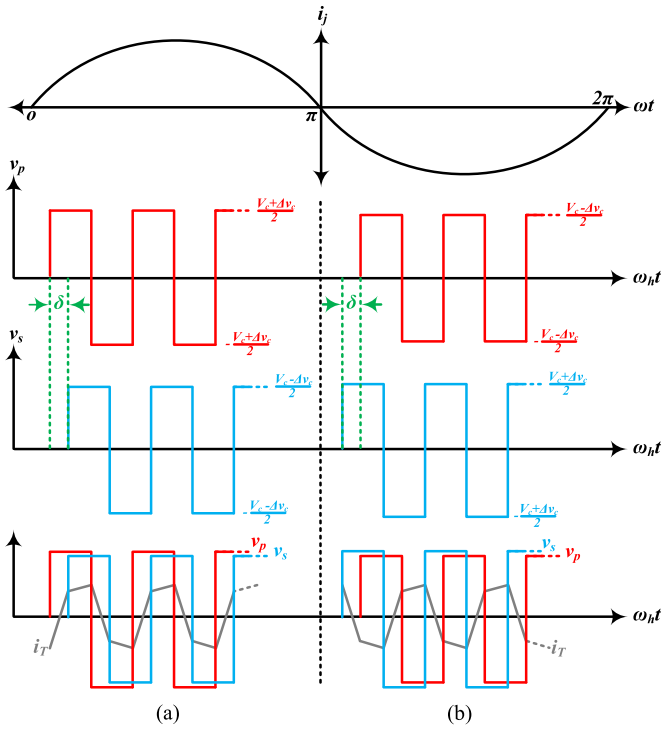

Fig. 6. Sketch map of the idealized waveforms of the DHB converter for bidirectional power transfer between front-to-front MMC SMs. (a) Positive phase-shift angle and (b) negative phase-shift angle.

left-side (primary side) SM, while at the same time, discharges the capacitor of a right-side (secondary side) SM.

Forward power transfer, designated as a positive phase shift, occurs during the positive half cycle of the MMC output current. In this case, the primary-side HB is the leading bridge, while the secondary-side HB is the lagging bridge. The same power transfer action is repeated during the negative half cycle of the output current but with the reversal of leading and lagging bridge sides, resulting in reverse power transfer, with a negative phase shift. This is elucidated in Fig. 6, where v_p and v_s are the voltages applied on the primary and secondary transformer sides, respectively, i_T is the transformer current, and ω_h is the angular frequency of the DHB switching devices. At any output current instant, the direction of power flow between front-to-front SMs in upper arms is opposite to that of front-to-front SMs in lower arms of the same dual leg.

B. Capacitor Voltage of the Proposed Dual MMC Configuration

With an appropriate control of the phase-shift angle of the DHB converters, the DM component of the pulsating power can be transferred from one SM to the adjacent one at the same voltage level, through HF transformer action. With the capacitor voltages of SMs, at both bridge sides, regulated to maintain their nominal value V_c, the DHB phase-shift angle allows the DM component of the pulsating power to be transferred from the SM interfaced with the leading bridge to the adjacent SM interfaced with the lagging bridge to counterbalance the same power component. That is, the DM component of the pulsating power is zero for each front-to-front SM, while the CM component is the same, as given by (8a). Therefore, the voltage fluctuation across SM capacitors in the dual MMC configuration is given by (16) with an absolute peak-to-peak value equal to the CM component, as shown in (17):

$$\Delta v_{c_{U\,j\ \text{proposed}}} = \Delta v_{c_{L\,j\ \text{proposed}}} = -\frac{I_o M}{16\omega C}\sin\left[2\left(\omega t+\theta_j\right)-\emptyset\right] \tag{16}$$

$$\Delta V_{c_{\text{proposed}}} = \Delta V_{c_{\text{cm}}} = \frac{I_o M}{8\omega C}. \tag{17}$$

Based on (17), the variation of the capacitor voltage ripple in the proposed dual MMC configuration inherits the same behavior of the CM component, shown in Figs. 2 and 3, which has the least influence on the capacitor voltage ripple.

The idealized waveforms of the SM capacitor voltage variation for a conventional MMC topology and the proposed dual MMC configuration are shown in Fig. 7, at the same SM capacitance and a nominal capacitor voltage of 2.5 kV. In Fig. 7(a), the capacitor voltage variation of a conventional MMC topology alternates with the fundamental line frequency, as a direct consequence of both CM and DM components, in an antiphase manner in the upper and lower arms, while the peak-to-peak voltage ripple is 440 V ($\pm 8.8\%$). On the other hand, the proposed dual MMC configuration features a second-order sinusoidal voltage variation across the SM capacitors, as shown in Fig. 7(b), which appears with the same phase in both upper and lower arms, with a peak-to-peak voltage fluctuation of 100 V ($\pm 2\%$).

Further assessment for the decreased capacitor voltage ripple is presented in Fig. 8, where the percentage reduction in the capacitor voltage ripple achieved by the proposed dual MMC configuration is depicted with respect to the capacitor voltage ripple of the conventional MMC topology, as the modulation index varies. The sizing requirement of the SM capacitance for both topologies is also compared in Fig. 8. The percentage capacitor voltage-ripple reduction is 60% at unity modulation index, with further improvement as the modulation index decreases. The ratio between SM capacitances, that result in the same capacitor voltage ripple, for a conventional MMC with respect to the proposed MMC configuration varies between two at unity modulation index, up to 50 times at low modulation indices. For simplicity, the reduction in the capacitor voltage ripple shown in Fig. 8 is calculated while considering only the DM component as the dominant voltage-ripple component for a conventional MMC topology.

C. Operation at Zero Motor Speed/Frequency

In a conventional MMC topology, the unidirectional current through MMC arms during near-zero-frequency power conversion results in a unidirectional change in SM capacitor voltage, leading to infinite capacitor voltage ripple. In contrast, one of the salient advantages of the proposed dual MMC configuration is that it has the capability of starting a machine at the full-load

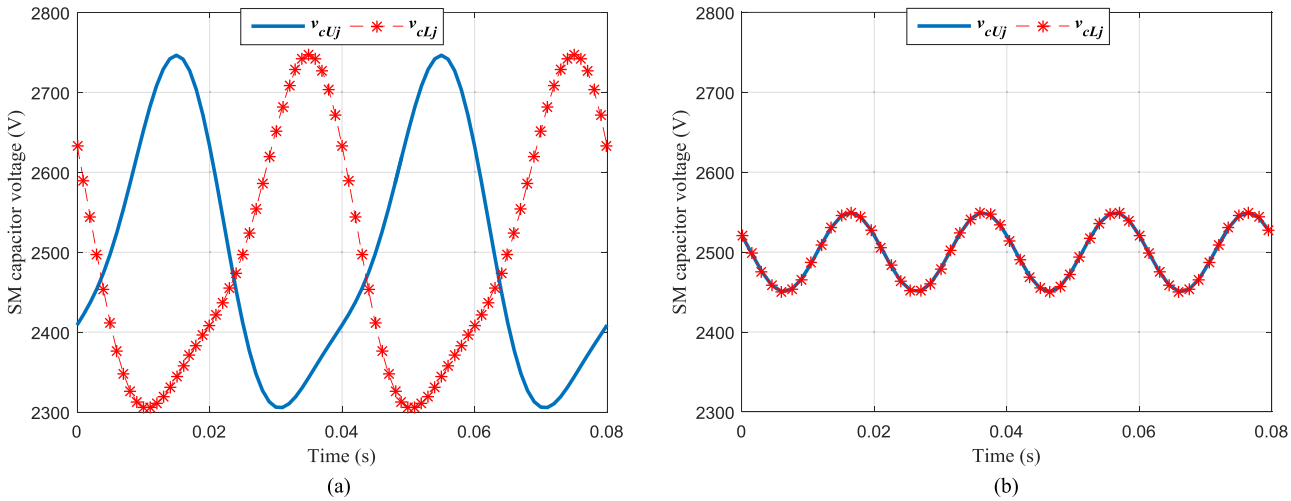

Fig. 7. Idealized waveforms of capacitor voltage variation for SMs in upper and lower arms ($C = 3$ mF, $f = 25$ Hz, $V_c = 2.5$ kV, $I_o = 500$ A, $M = 0.75$, and $\emptyset = 25°$). (a) Conventional MMC topology and (b) proposed dual MMC configuration.

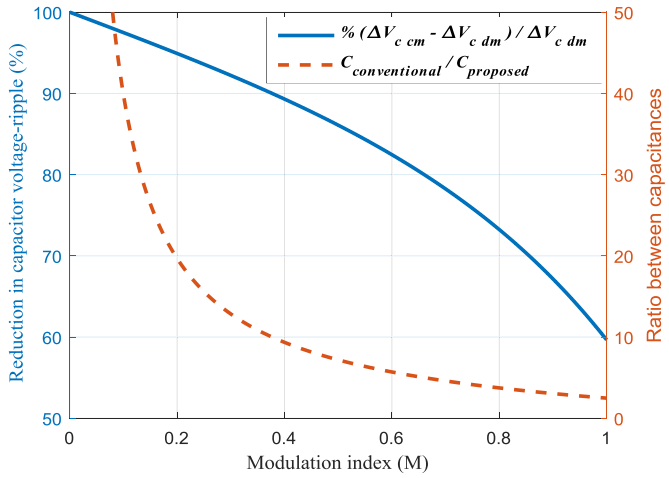

Fig. 8. Assessment of voltage-ripple reduction and SM capacitance size for conventional MMC and the proposed MMC configuration ($\emptyset = 25°$).

torque from a standstill condition with a ripple-free SM capacitor voltage profile. That is, at near-zero frequency, the power drawn at the output side will be near dc power, and, therefore, the CM component of the pulsating power in MMC arms will be zero. Also, with unidirectional transfer of the dc DM power component between front-to-front SMs in both the upper and lower arms, the resultant pulsating power in different arms will be zero. In this case, the capacitive energy stored in the MMC arms will be redistributed evenly at a constant level among all SMs, resulting in a constant voltage across SMs' capacitors.

D. DHB Design Guidelines

1) Transformer Leakage Inductance: Referring to (15), transformer power transferred is governed by the phase-shift angle and transformer leakage inductance when the DHB's switching frequency is constant. The maximum power transfer occurs when the phase-shift angle $\sigma = 1/2\pi$. Therefore, the maximum power transfer is

$$P_{T_{\max}} = \frac{{V_c}^2}{32 f_h L}. \tag{18}$$

Since the DM component of the arm power alternates as shown in (8b), the maximum amplitude of the decoupled DM power component for each front-to-front SM is

$$P_{\mathrm{dm_{SM}}} = \frac{V_{\mathrm{dc}}\, I_o}{4N}. \tag{19}$$

The peak decoupled power of each pair of adjacent SMs must be less than the maximum power-transfer ability of the transformer. Substituting $P_{\mathrm{dm_{SM}}} \leq P_{T_{\max}}$ gives a boundary condition for the transformer leakage inductance

$$L \leq \frac{V_{\mathrm{dc}}}{8N I_o f_h}. \tag{20}$$

2) Ratings of the Transformer: The voltage applied on both transformer windings is $\frac{1}{2}V_c$, while the maximum transformer current is related to the peak value of the decoupled DM power, where it is limited to half the amplitude of the output current, and is given by

$$I_{T_{\max}} = \frac{2P_{\mathrm{dm_{SM}}}}{V_c} = 1/2I_o. \tag{21}$$

3) Ratings of Switching Devices: The voltage rating of the DHB switching devices is V_c, while the current rating is $\frac{1}{2}I_o$.

IV. Simulation Verification

The effectiveness of the proposed dual MMC configuration with DHB energy balancing modules is verified through simulation studies at different operating conditions. A 10-MW MATLAB/SIMULINK model is used to investigate the steady-state operation of the proposed dual MMC configuration with a brief comparison to the traditional single-sided MMC topology, while a 100-MW model is considered to investigate the dynamic performance of the proposed configuration when the operating frequency is increased from zero up to the rated frequency at rated

TABLE I
PARAMETERS FOR SIMULATION

Parameters of proposed MMC configuration	
Number of SMs per arm (N)	5
Input dc voltage ($V_{\rm dc}$)	12.5 kV
Average voltage across SM capacitor (V_c)	2.5 kV
Rated output voltage	8 kV
Fundamental output frequency (f_o)	50 Hz
Carrier frequency of MMC (f_c)	2 kHz
Switching frequency of DHB (f_h)	10 kHz
Parameters for steady-state operation using *RL* load	
Rated active power	10 MW
Rated current magnitude (I_o)	655 A
Load resistance	$15.5 \times \frac{f_o}{50}\ \Omega$
Load inductance	24 mH
Arm inductance ($L_{\rm arm}$)	2 mH
Equivalent SM series capacitance (C)	1 mF
Parameters for transient operation using an open-end winding motor	
Rated active power	100 MW
Number of poles	10
Rated motor speed	600 r/min
Rated phase voltage	8 kV
Arm inductance ($L_{\rm arm}$)	2.4 mH
Equivalent SM series capacitance (C)	2 mF

current. Simulation parameters for both models are listed in Table I, while simulation results are presented in Figs. 9–14.

A. Simulation Results With an RL Load

Figs. 9 and 10 show the fundamental waveforms of 10-MW steady-state operation for both proposed and traditional MMC configurations at both rated output current and frequency in Table I. In Fig. 9, the proposed dual MMC configuration feeds three-phase *RL* load connected in an open-end configuration via three-paralleled dual legs, each with five SMs per arm, supplied from a 12.5-kV dc input voltage. In Fig. 10, the traditional MMC feeds a three-phase star-connected *RL* load via three conventional single legs, each of ten SMs per arm, supplied from a 25-kV dc input voltage. For both configurations, the modulation index is set to 0.904 to generate an 8-kV output phase voltage (13.8-kV line-to-line voltage for the single-sided configuration). Comparing the results in Figs. 9 and 10, the differential output voltage across the terminals of the open-end load $v_{jj'}$ in the dual-sided configuration has half the number of voltage levels compared to the phase voltage v_{jo} of the single-sided topology. Nonetheless, the quality of the output currents for both configurations are near the same, with a current peak equal to the rated value of 655 A. In both configurations, the currents in upper and lower arms are controlled to suppress both second- and fourth-order harmonic components to give a nearly constant CM current as assumed in the mathematical analysis in Section II. The recorded peak arm current is 510 A while the average CM current is 135 A, for both configurations. The capacitor voltage ripple of the proposed dual MMC alternates at twice the line frequency with a voltage ripple constitutes for $\pm 6\%$ using an equivalent SM capacitance of 1 mF. Whereas the capacitor voltage ripple in the traditional MMC alternates at the fundamental

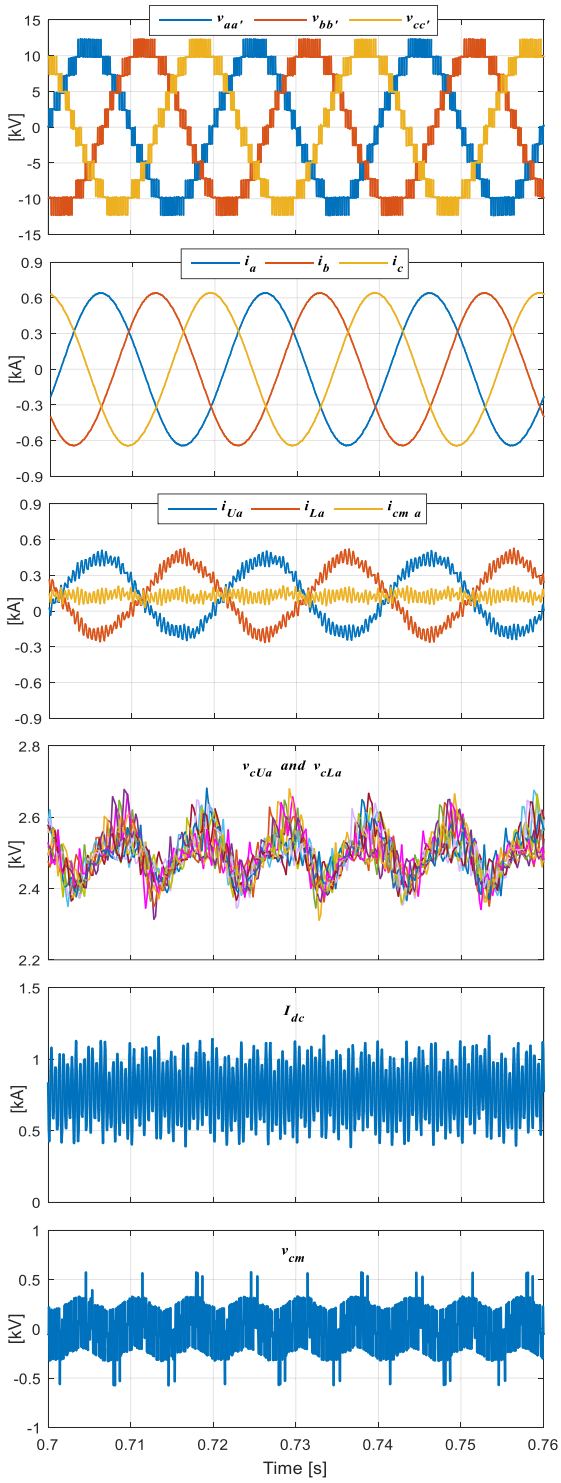

Fig. 9. Fundamental simulation waveforms for a steady-state operation of the proposed dual MMC configuration at 50 Hz.

frequency as a consequence of the contribution of both CM and DM ripple components. The voltage ripple of the traditional MMC is $\pm 7.8\%$, while the SM capacitance is 2 mF. The current drawn from the input supply $\boldsymbol{I}_{\rm dc}$ is doubled in the dual-sided topology compared to the single-sided topology since the former operates at half the dc input voltage. The CM voltage of the dual-sided topology is shown to be slightly lower than that of

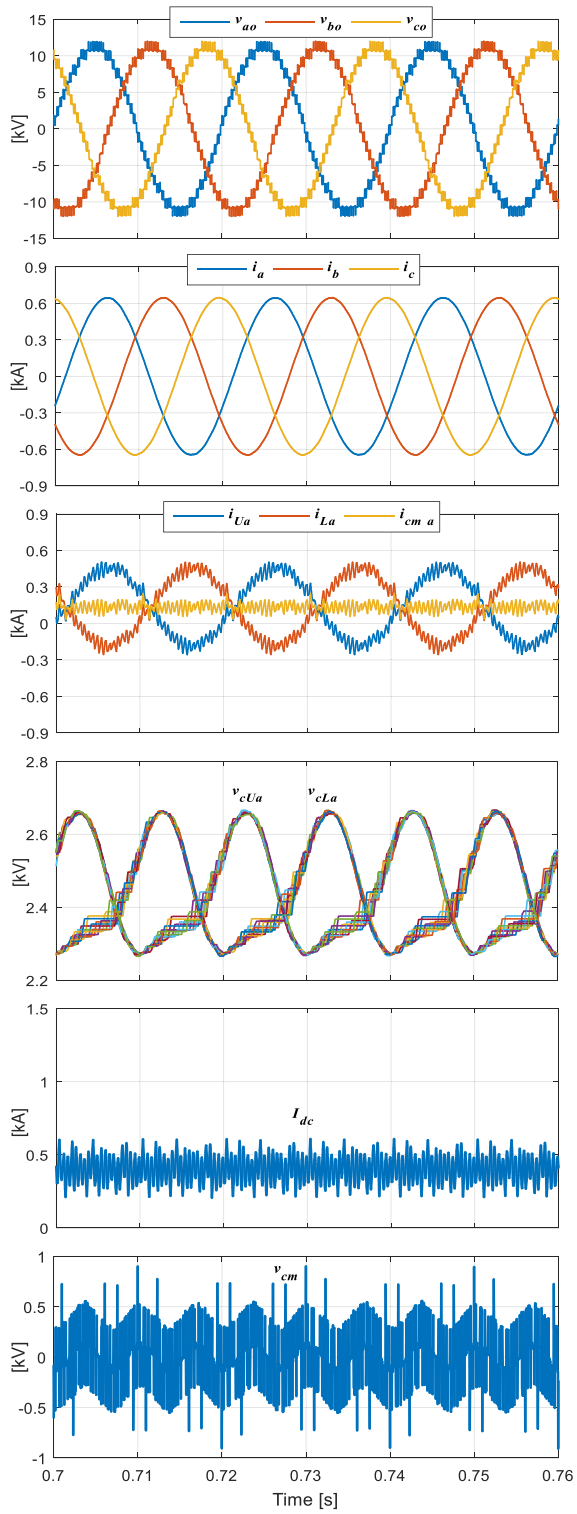

Fig. 10. Fundamental simulation waveforms for a steady-state operation of a traditional single-sided MMC at 50 Hz.

the single-sided topology due to the exploitation of the available redundant states offered by dual-sided configurations.

Fig. 11 shows the voltage across each side of the HF transformer along with the transformer current during positive and negative half cycles of the output current. The voltage across both sides is near 1.25 kV which is half the nominal SM capacitor voltage. In Fig. 11(a), the voltage at the primary side is higher than the voltage at the secondary side with a leading phase shift, where the waveforms are recorded while the arm current is charging the capacitors connected to the primary side, and discharging the capacitors connected to the secondary side, resulting in a forward power transfer from the primary to the secondary side. The opposite case is shown in Fig. 11(b), where the primary voltage lags with a lower magnitude than the secondary voltage, producing a reverse power transfer, from the secondary to the primary side.

Fig. 12 shows the performance of the proposed dual MMC configuration when operated at low frequencies, according to a Volt/Hertz control scheme. From left to right, the results of Fig. 12 are obtained for continuous operation at 10, 5, and 1 Hz, respectively. In this case study, the output voltage is reduced in accordance to the operating frequency reduction, while the load resistance is varied linearly with the operating frequency to maintain the output current constant at the rated value, at all frequencies, to emulate the constant torque characteristic of variable-speed motors. The output currents are high-quality sinusoidal waveforms with a peak of 655 A, while the arm currents are maintained free of dominant even-harmonic components. Importantly, the SM capacitor voltages are balanced and not affected by the reduction in both modulation index and operating frequency. The voltage ripple across the SMs' capacitors is $\pm 5\%$, while the equivalent SM capacitance is 1 mF.

To assess the reduction in capacitor voltage ripple achieved by the proposed configuration, Fig. 13 shows capacitor voltage-variation with deactivation of the DHB switching signals at the mid-period of a simulation at low operating frequencies. When the DHB PWM signals are inhibited, the configuration is reduced to a conventional dual-sided MMC which inherits the same capacitor voltage-ripple profile as the single-sided MMC. At the time of deactivation of the energy-balancing modules, the capacitor voltage ripple significantly increases especially as the operating frequency is further reduced. While the voltage ripple of the SMs' capacitors is near constant at $\pm 5\%$ at the three-different frequencies when the DHB modules are in operation, the voltage ripple after DHB deactivation is recorded at $\pm 33\%$, $\pm 50\%$, and $\pm 66\%$ at 10, 5, and 1 Hz, respectively. Although the latter voltage-ripple percentages are impractically high, they highlight the significant reduction in the sizing requirement of SM capacitance, which could be achieved by counterbalancing the DM ripple power between adjacent-arm SMs of the dual MMC legs through the incorporation of DHB modules.

B. Simulation Results With an Open-End Winding Machine

To investigate the dynamic performance of the proposed dual MMC configuration and to establish its ability to extend the output power to scores of megawatts, Fig. 14 presents the dynamic performance of a 100-MW 8-kV open-end winding motor, while driven from standstill to the rated speed at full-load torque. The results in Fig. 14 show that the output currents are of high quality over the whole speed range, while the SM capacitor voltages are balanced with a bounded voltage ripple regardless of the operating frequency. Also, the dual MMC configuration is able

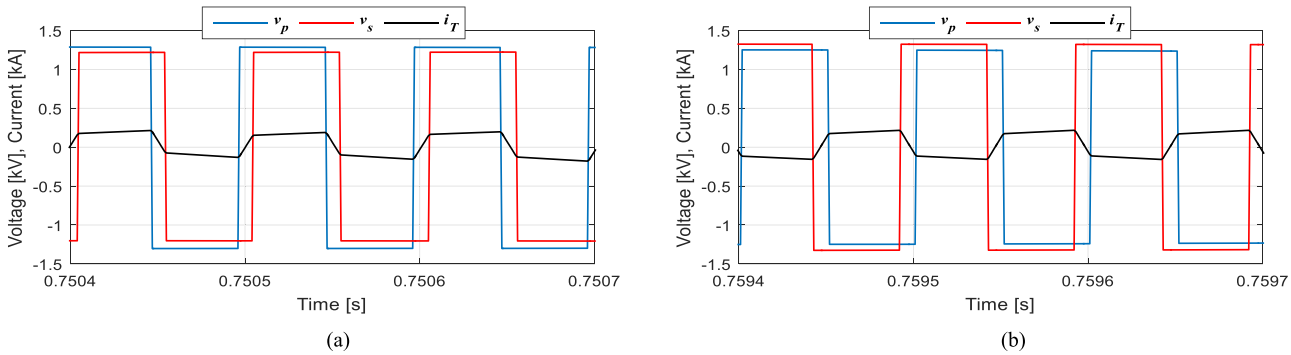

Fig. 11. Key waveforms of the phase-shift DHB converter. (a) Primary voltage is leading and (b) primary voltage is lagging.

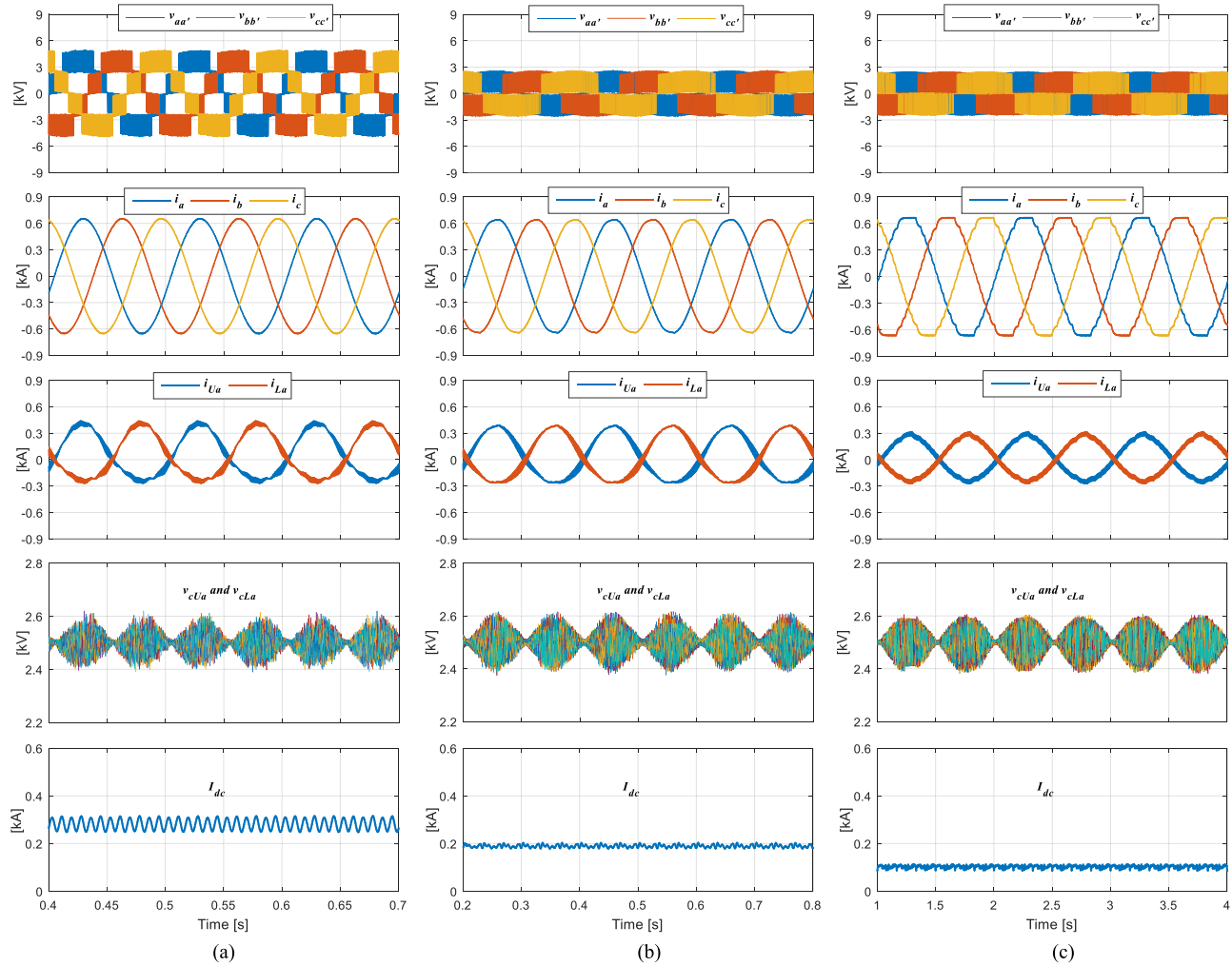

Fig. 12. Simulation results for a continuous operation of the proposed dual MMC topology at (a) 10 Hz, (b) 5 Hz, and (c) 1 Hz.

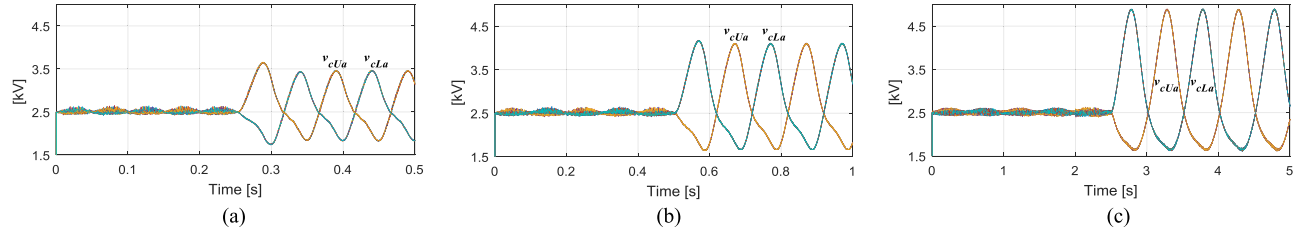

Fig. 13. Simulation results for capacitor voltage fluctuation of the proposed dual MMC topology with deactivation of DHB modules at mid-simulation time at (a) 10 Hz, (b) 5 Hz, and (c) 1 Hz.

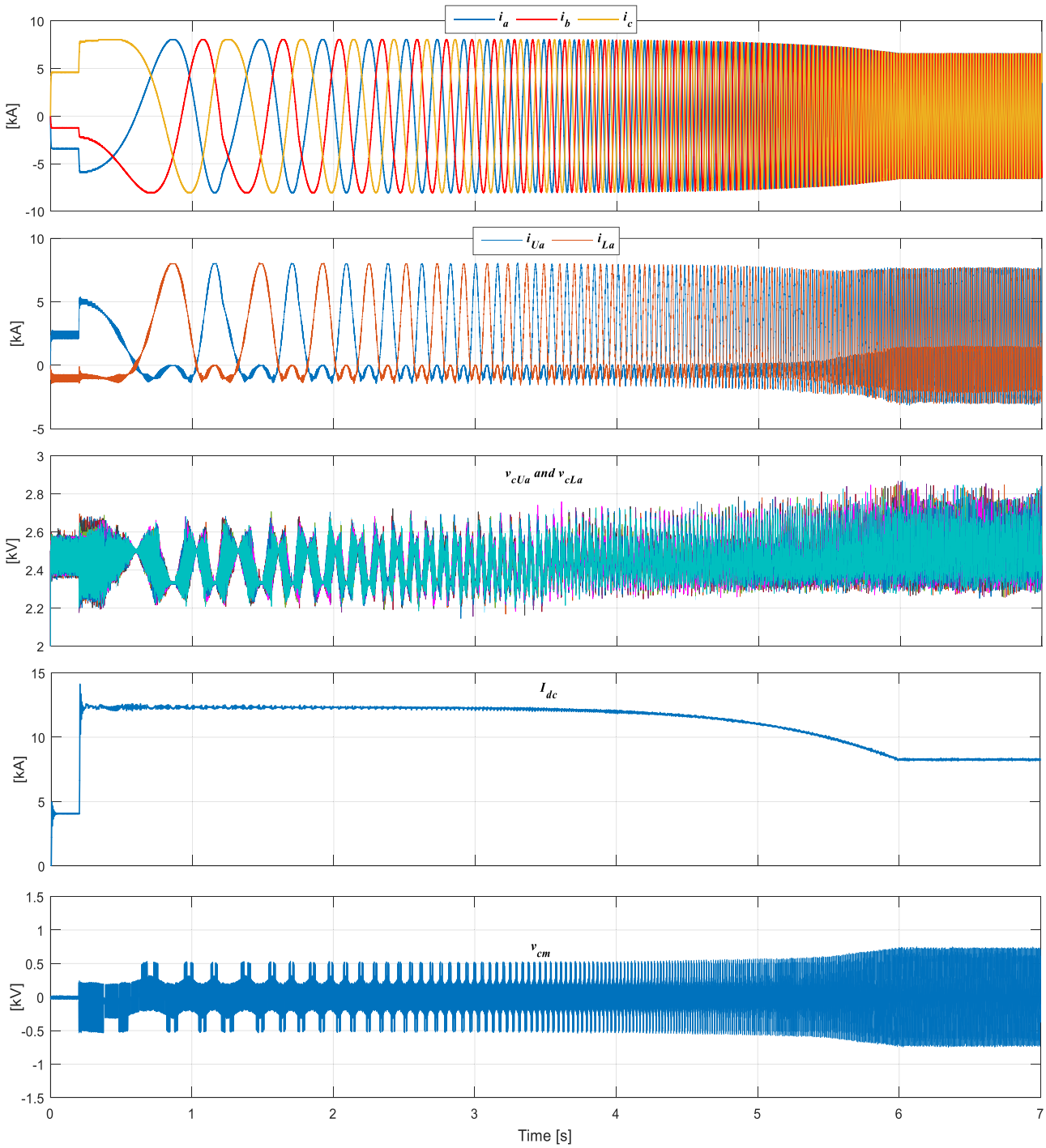

Fig. 14. Simulation of transient operation of the proposed dual MMC configuration when driving an open-end stator winding motor from standstill to the rated speed at constant full-load torque.

to operate at near-zero frequency, with a constant SM capacitor voltage ripple. It is worth noting that the capacitor voltage ripple is slightly increasing at frequencies near the rated frequency compared to the voltage ripple at low frequencies, where the voltage ripple varies between $\pm 1\%$ at near 0 Hz and $\pm 10\%$ at 50 Hz. The increase in the capacitor voltage ripple at higher motor speeds is due to the growth of the CM current which in turn increases the CM voltage-ripple component.

V. Experimental Verification

A scaled-down prototype of the proposed dual MMC configuration with DHB energy-balancing modules is built to practically verify the effectiveness of the proposed concept. The experimental prototype has three SMs per arm (12 SMs for each dual leg), rated at 4 kW and 210 V. The dc-link voltage is 300 V, and the nominal SM capacitor voltage is 100 V.

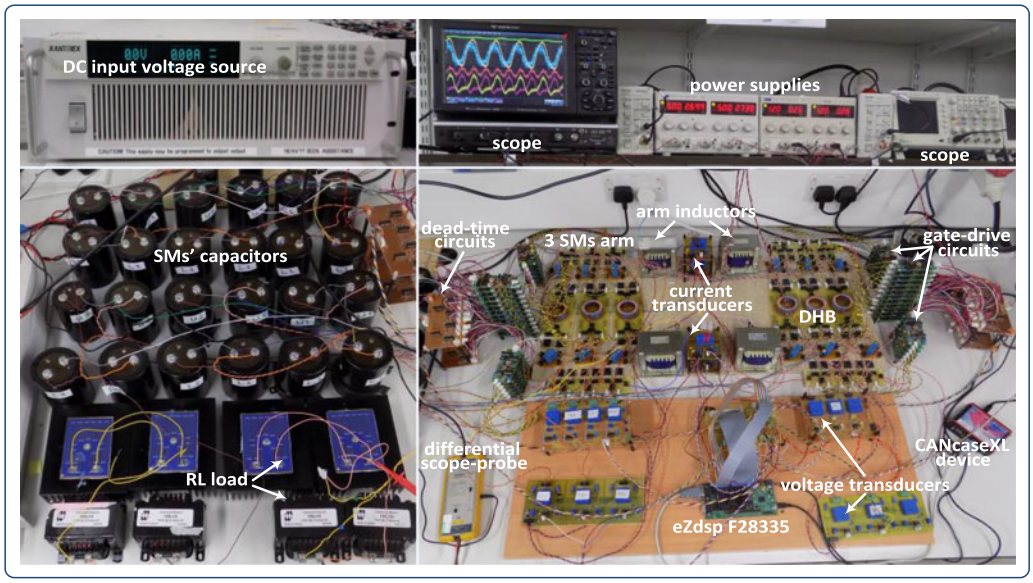

Fig. 15. Scaled-down experimental setup.

TABLE II
PARAMETERS FOR EXPERIMENTATION

Number of SMs per arm (N)	3
Rated active power	4 kW
Input dc voltage ($V_{\rm dc}$)	300 V
Rated current magnitude (I_o)	9.5 A
Average voltage across SM capacitor (V_c)	100 V
Fundamental output frequency (f_o)	50 Hz
Carrier frequency of MMC (f_c)	2 kHz
Switching frequency of DHB (f_h)	10 kHz
Load resistance	$30 \times \frac{f_o}{50}\ \Omega$
Load inductance	20 mH
Arm inductance ($L_{\rm arm}$)	2.8 mH
Equivalent SM series capacitance (C)	1.1 mF
Transformer turns ratio (n)	1
Auxiliary leakage inductance (L)	100 μH

Front-to-front SMs are interfaced through DHB converters employing a nanocrystalline core-based HF transformer with a saturation flux density of 1.2 T and a unity turns ratio. The control system is implemented in a TMS320F28335 DSP. The main units employed in the experimental setup are shown in Fig. 15, while the parameters and operating conditions are listed in Table II. Three-phase *RL* loads, connected in an open-end configuration, were connected to the dual MMC topology to assess its steady-state performance at different operating frequencies starting from the rated frequency down to 1 Hz, while the load resistance was varied linearly with the output frequency to emulate the constant torque condition of an induction motor. Results were recorded during both activation and deactivation of the DHB modules to confirm the influence of the proposed configuration. Experimental results are presented in Figs. 16–22.

Fig. 16 shows the differential voltages across two phases of the open-end load terminals ($v_{aa'}$ and $v_{bb'}$) and their currents (i_a and i_b) when the proposed MMC configuration is operated

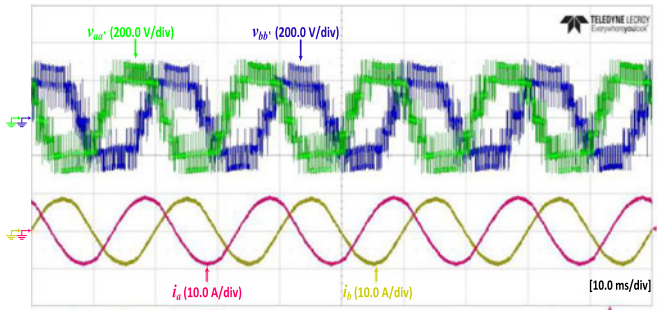

Fig. 16. Voltage and current waveforms for a steady-state operation of the proposed dual MMC configuration at 50 Hz.

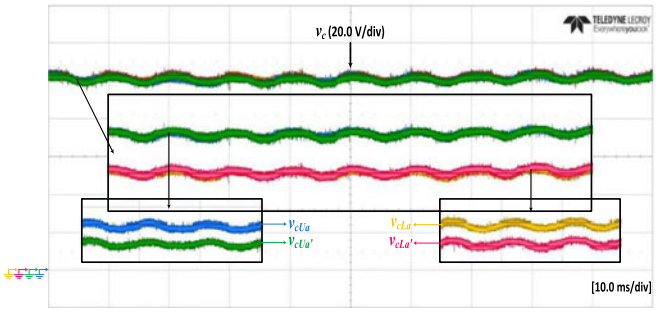

Fig. 17. Voltages across SM capacitors at 50 Hz.

at 50 Hz and 0.9 modulation index. The output voltages have three voltage levels with a peak of the dc input voltage, while the output currents are high quality with a magnitude of 9.5 A. Since the three-phase configuration is balanced, the differential voltage $v_{cc'}$ and the load current i_c will have $2/3\pi$ phase displacement. Fig. 17 shows samples of SM capacitor voltages in the four arms of the dual phase leg aa' where they are balanced around 100 V, while alternating at twice the line frequency due to the CM component of the capacitor voltage ripple.

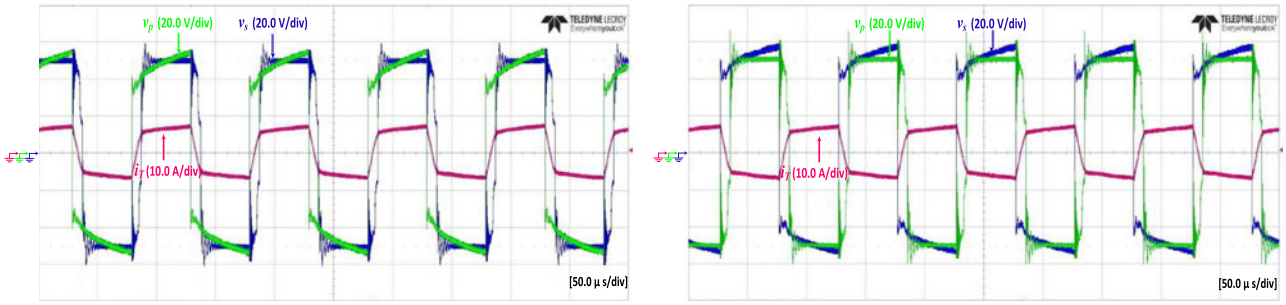

(a) (b)

Fig. 18. Fundamental switching waveforms of the phase-shift DHB converter. (a) Forward power flow and (b) reverse power flow.

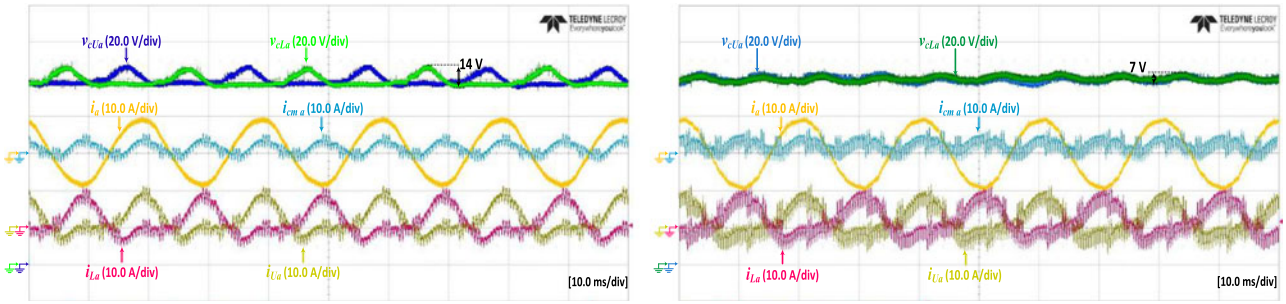

(a) (b)

Fig. 19. Experimental results at 50 Hz when DHB modules are (a) deactivated and (b) activated.

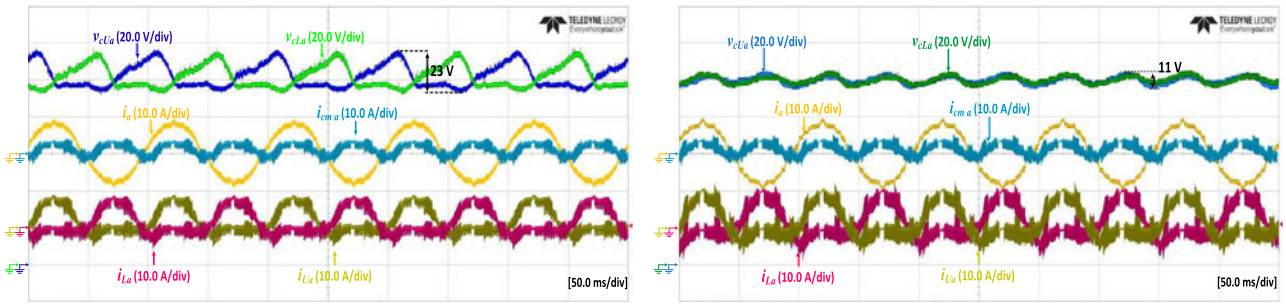

(a) (b)

Fig. 20. Experimental results at 10 Hz when DHB modules are (a) deactivated and (b) activated.

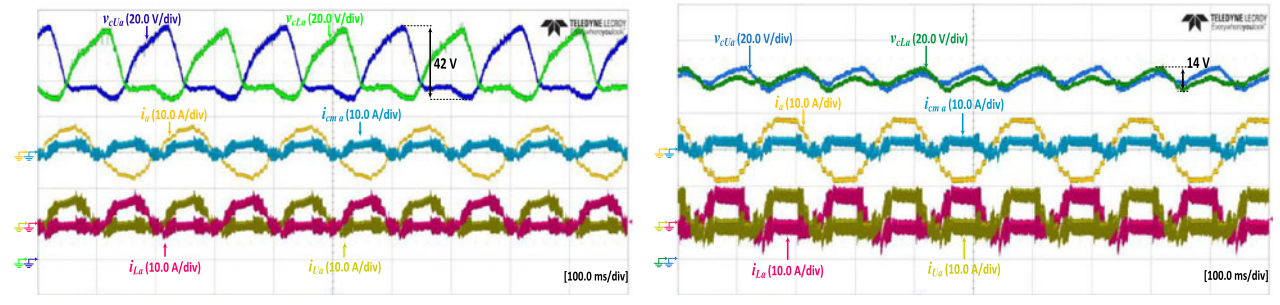

(a) (b)

Fig. 21. Experimental results at 5 Hz when DHB modules are (a) deactivated and (b) activated.

The fundamental switching waveforms of the phase-shift DHB converter in Fig. 18 show the voltages across both transformer sides in addition to the transformer current during both forward and reverse power flows. The DHB converter is operating at 10 kHz, while an auxiliary inductance of 100 μH is connected in series with the transformer primary side. Both primary- and secondary-side voltages are square waveforms with a constant duty cycle of 50%, and near 50-V peak which

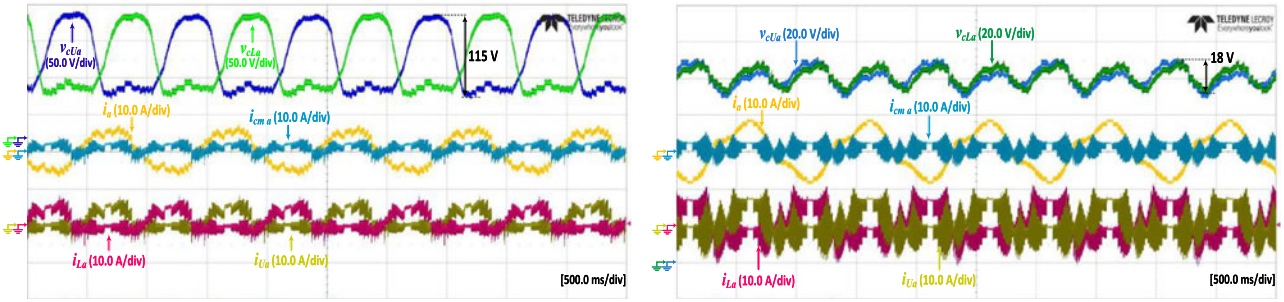

Fig. 22. Experimental results at 1 Hz when DHB modules are (a) deactivated and (b) activated.

is half the nominal voltage across each SM capacitor. Also, the peak transformer current is near 6 A.

The experimental results of the dual MMC configuration that assess the SM capacitor voltage ripple at different operating frequencies are presented in Figs. 19–22 with suffix "a" when the DHB modules are deactivated, while suffix "b" means the DHB modules are operational. Only the voltage of one SM from each arm is shown, since the other waveforms are virtually identical, in addition to the output current, arm currents, and the CM current. The output voltage is reduced in accordance to operating frequency reduction, while the load resistance is varied linearly with the operating frequency to maintain constant rated output current. When the DHB modules are deactivated in the proposed MMC configuration, it exhibits the performance of a traditional MMC. At 50 Hz, Fig. 19 shows that the capacitor voltage ripple of a traditional MMC is 14 V (±7%), while it is reduced to 7 V (±3.5%) when the DHB modules are activated. In both cases, the output current is regulated at the rated value, while the CM current includes second-order harmonics, since the CM current has not been controlled to experimentally suppress even-order harmonics, so clearly affects both arm current waveforms. In Fig. 20, the operating frequency is reduced to 10 Hz where the capacitor voltage ripple is 23 V (±11.5%) for a traditional MMC, and 11 V (±5.5%) with DHB activation. With further operating frequency reduction to 5 Hz (see Fig. 21) and 1 Hz (see Fig. 22), the capacitor voltage ripple is significantly increased to 42 V (±21%) and 115 V (±57.5%), respectively, for a traditional MMC topology, while being 14 V (±7%) and 18 V (±9%), respectively, with DHB modules operation. As the operating frequency is reduced, the output current of the traditional MMC can no longer be controlled at the rated value, since the increased capacitor voltage ripple results in a loss of controllability. In contrast, the output current of the proposed MMC configuration is always regulated at the rated value, regardless of the operating frequency, as shown in Figs. 19–22. The quality of the load current waveforms is adversely affected with the operating frequency reduction since the number of voltage levels is reduced. The percentage reduction in the capacitor voltage ripple, and, hence, the reduction in the required SM capacitance, gained by the activation of the DHB modules is found to be 66% and 84% at 5 and 1 Hz, respectively, although the output currents are much lower than the rated value when the DHB modules are deactivated at these low operating frequencies.

VI. Assessment of the Proposed MMC Configuration

Compared with the currently accepted MMC topologies and circulating-current control approaches, the proposed dual MMC configuration is characterized as an innovative solution able to drive MV multimegawatt open-end winding machines at full-load torque, in an independent scheme of the operating frequency, even at zero speed/frequency. The proposed configuration inserts DHB modules, between each front-to-front SM of the same dual leg, that form an auxiliary branch for the dual MMC topology to maintain the SM capacitor voltage balance over whole frequency range. Therefore, the proposed configuration has a power branch and an auxiliary balance branch, with the former to perform the necessary power conversion, while the latter to decouple the fundamental ripple-power component to maintain voltage balance between the SMs. It is worth mentioning that the proposed configuration still retains the modularity feature since the auxiliary balance branches have a modular scheme. In addition, there is no interaction between the control of the DHB modules and the basic control loops of the MMC.

The decoupling of the fundamental ripple-power component between front-to-front SMs, through the DHB units, results in a reduction in the SM capacitance. The DHB hardware adds volume to the MMC system, countering the capacitance reduction. Aside from the two added switching devices for each MMC SM, the inserted transformer between front-to-front SMs is an energy transfer element, and does not increase MMC stored energy. Thus, the DHB with the reduced SM capacitance reduces system stored energy.

The proposed MMC configuration has a dc-fault-blocking capability. With the inhibition of the PWM signals of the switching devices at the fault instant, the proposed configuration produces a zero differential voltage across the machine windings, while the SM capacitors do not contribute to the fault current.

Considering the efficiency of the proposed MMC configuration, the four switching devices of the DHB converter in addition to the HF transformer inevitably increase the power loss and reduce the efficiency of the overall system when compared

to a conventional MMC topology. However, since conventional MMC topologies cannot drive multimegawatt machines at very low speeds, accurate power loss analysis will be investigated in future research to compare the efficiency of the proposed MMC configuration with the efficiency of MMC topologies that utilize HF circulating-current injection approaches.

A comparison of the proposed MMC configuration with the conventional MMC topology in terms of component volume is presented for 10-MW system selected as the case study. Since the number of SMs is the same, and identical, so the comparison is conducted for only one SM.

A. Switching Devices

For the power branch, the 5SNA1200G450350 IGBT with 4.5-kV 1200-A power rating is chosen [55], while the balancing branch can utilize 5SNA0650J450300 IGBTs with 4.5 kV 650 A [56], both from ABB. The volume of the power branch and balancing branch IGBTs is 1.28 and 0.87 L, respectively. For conventional MMC topology, two power-branch IGBTs are required, while the proposed MMC configuration requires two balancing-branch IGBTs in addition to the conventional two power-branch IGBTs. As a result, the volume of the switching devices is increased by 68%.

B. SM Capacitors

Each SM in the proposed MMC configuration requires two 2-mF 1.4-kV capacitors. This capacitance enables the proposed MMC configuration to operate the 10-MW system continuously at any operating frequency, even at near-zero frequency, with a near constant $\pm 5\%$ capacitor voltage ripple. To achieve the same voltage-ripple suppression effect, according to the simulation results in Fig. 13(c) at 1 Hz, the capacitance of the conventional MMC topology should be 13 times of the equivalent SM capacitance of the proposed MMC configuration. Therefore, the conventional MMC topology requires one capacitor with 13 mF and 2.8 kV, while being unable to drive such 10-MW system at near-zero frequency. The capacitive energy stored in each SM in case of the conventional MMC topology is 51 kJ, while it is only 4 kJ for the proposed MMC configuration. Accordingly, the percentage reduction in the capacitive stored energy achieved by the proposed MMC configuration is 92%. To assess the reduction in the capacitors size, according to the oil-impregnated power capacitors from EPOCS [57], the volume of capacitors combination required to match the parameters of the SM capacitor of a conventional MMC is 440 L, while the volume of the SM split capacitor for the proposed MMC configuration is only 38 L, with a 91% volume reduction.

C. HF Transformer

For a full decoupling of the fundamental ripple-power component, each front-to-front SM requires an HF transformer with 1:1 turns ratio and 1.25-kV 330-A power rating. An estimation for the transformer size can be obtained based on practical assemblies for HF transformers designed for high-power applications in previous studies [58]–[60], where the transformer volume for the mentioned ratings could be 17 L.

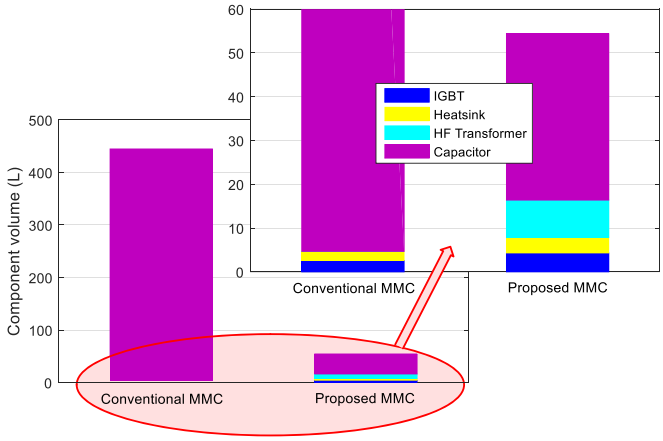

Fig. 23. Component volume comparison per SM for both conventional and proposed MMC.

Fig. 23 compares the volume of the main components of each SM for both MMC approaches. By using the proposed MMC configuration, the component volume can be reduced from 445 to 55 L, resulting in 87% reduction in the overall SM volume. It should be noted that this is only a comparison for the volume of the main SM components (capacitor, HF transformer, IGBT, and heat sink), rather than a comparison of the volume of real SM enclosures (in which there are more components). Nevertheless, a significant decrease in the main component volume enables a more compact and lighter layout design of an SM enclosure.

VII. Conclusion

A novel configuration for MV high-power machine drives incorporating open-end stator windings has been proposed based on a dual MMC topology. The configuration is characterized by the insertion of HF transformer-based bidirectional dc–dc converter units between front-to-front MMC SMs operating in the same dual leg. Based on the fact that the fundamental ripple power of adjacent-arm SMs in dual MMC topology alternates with an opposite phase, the dc–dc converter modules can decouple this fundamental ripple power, allowing the capacitive stored energy to be evenly distributed among all SMs. The main advantages of the proposed configuration are summarized as follows. It offers 1) a significant reduction in SM capacitance since the voltage fluctuations across the capacitors are brought down to a very narrow band, therefore reducing the energy stored in the converter system. 2) Eliminates the problems of capacitor voltage fluctuations in an independent operating frequency scheme. 3) A single dc-source operation with half the value of the dc input voltage compared to single-sided converter configurations, in addition to the higher redundant space vector combinations that are utilized in CM voltage elimination. 4) A dc-fault-blocking capability. 5) Compared to circulating-current injection methods, the proposed configuration does not affect the arm current or the CM voltage. The proposed configuration is believed to be the most suitable solution for adjustable-speed drives since it guarantees the continuous operation at any speed/torque

condition with the ability of driving multimegawatt machines from standstill at full-load torque.

Minor drawbacks countering the mentioned advantages are 1) the proposed configuration utilizes extra hardware which slightly reduces the MMC system efficiency. 2) It necessitates each MMC SM to have a split capacitor bank.

The proposed configuration has been examined for MV high-power adjustable-speed drive applications through mathematical analysis and simulations. Theoretical deductions were validated by experimentation, which agreed with theoretical analysis and simulation.

REFERENCES

[1] A. Lesnicar and R. Marquardt, "An innovative modular multilevel converter topology suitable for a wide power range," in *Proc. IEEE Power Tech Conf.*, Bologna, Italy, vol. 3, Jun. 23–26, 2003.

[2] M. A. Perez, S. Bernet, J. Rodriguez, S. Kouro, and R. Lizana, "Circuit topologies, modeling, control schemes, and applications of modular multilevel converters," *IEEE Trans. Power Electron.*, vol. 30, no. 1, pp. 4–14, Jan. 2015.

[3] S. Debnath, J. Qin, B. Bahrani, M. Saeedifard, and P. Barbosa, "Operation, control, and applications of the modular multilevel converter: A review," *IEEE Trans. Power Electron.*, vol. 30, no. 1, pp. 37–53, Jan. 2015.

[4] H. Akagi, "Classification, terminology, and application of the modular multilevel cascade converter (MMCC)," *IEEE Trans. Power Electron.*, vol. 26, no. 11, pp. 3119–3130, Nov. 2011.

[5] L. Harnefors, A. Antonopoulos, S. Norrga, L. Angquist, and H.-P. Nee, "Dynamic analysis of modular multilevel converters," *IEEE Trans. Ind. Electron.*, vol. 60, no. 7, pp. 2526–2537, Jul. 2013.

[6] M. Saeedifard and R. Iravani, "Dynamic performance of a modular multilevel back-to-back HVDC system," *IEEE Trans. Power Del.*, vol. 25, no. 4, pp. 2903–2912, Oct. 2010.

[7] M. Guan and Z. Xu, "Modeling and control of a modular multilevel converter-based HVDC system under unbalanced grid conditions," *IEEE Trans. Power Electron.*, vol. 27, no. 12, pp. 4858–4867, Dec. 2012.

[8] A. Hassanpoor, A. Roostaei, S. Norrga, and M. Lindgren, "Optimization-based cell selection method for grid-connected modular multilevel converters," *IEEE Trans. Power Electron.*, vol. 31, no. 4, pp. 2780–2790, Apr. 2016.

[9] J. Peralta, H. Saad, S. Dennetiere, J. Mahseredjian, and S. Nguefeu, "Detailed and averaged models for a 401-level MMC–HVDC system," *IEEE Trans. Power Del.*, vol. 27, no. 3, pp. 1501–1508, Jul. 2012.

[10] M. Hagiwara, K. Nishimura, and H. Akagi, "A medium-voltage motor drive with a modular multilevel PWM inverter," *IEEE Trans. Power Electron.*, vol. 25, no. 7, pp. 1786–1799, Jul. 2010.

[11] S. Busquets-Monge, S. Somavilla, J. Bordonau, and D. Boroyevich, "Capacitor voltage balance for the neutral-point-clamped converter using the virtual space vector concept with optimized spectral performance," *IEEE Trans. Power Electron.*, vol. 22, no. 4, pp. 1128–1135, Jul. 2007.

[12] S. Thielemans, A. Ruderman, B. Reznikov, and J. Melkebeek, "Improved natural balancing with modified phase-shifted PWM for single-leg five-level flying-capacitor converters," *IEEE Trans. Power Electron.*, vol. 27, no. 4, pp. 1658–1667, Apr. 2012.

[13] S. Du, J. Liu, and J. Lin, "Hybrid cascaded H-bridge converter for harmonic current compensation," *IEEE Trans. Power Electron.*, vol. 28, no. 5, pp. 2170–2179, May 2013.

[14] A. Korn, M. Winkelnkemper, and P. Steimer, "Low output frequency operation of the modular multi-level converter," in *Proc. IEEE Energy Convers. Congr. Expo.*, 2010, pp. 3993–3997.

[15] S. Debnath, J. Qin, and M. Saeedifard, "Control and stability analysis of modular multilevel converter under low-frequency operation," *IEEE Trans. Ind. Electron*, vol. 62, no. 9, pp. 5329–5339, Sep. 2015.

[16] J. Kolb, F. Kammerer, M. Gommeringer, and M. Braun, "Cascaded control system of the modular multilevel converter for feeding variable-speed drives," *IEEE Trans. Power Electron.*, vol. 30, no. 1, pp. 349–357, Jan. 2015.

[17] M. Spichartz, V. Staudt, and A. Steimel, "Modular multilevel converter for propulsion system of electric ships," in *Proc. IEEE Electr. Ship Technol. Symp.*, 2013, pp. 237–242.

[18] A. Antonopoulos, L. Angquist, S. Norrga, K. Ilves, L. Harnefors, and H.-P. Nee, "Modular multilevel converter ac motor drives with constant torque from zero to nominal speed," *IEEE Trans. Ind. Appl.*, vol. 50, no. 3, pp. 1982–1993, May/Jun. 2014.

[19] J. Jung, H. Lee, and S. Sul, "Control of the modular multilevel converter for variable-speed drives," in *Proc. IEEE Int. Conf. Power Electron., Drives Energy Syst.*, Bengaluru, India, Dec. 16–19, 2012, pp. 1–6.

[20] K. Wang, Y. Li, Z. Zheng, and L. Xu, "Voltage balancing and fluctuation-suppression method of floating capacitors in a new modular multilevel converter," *IEEE Trans. Ind. Electron.*, vol. 60, no. 5, pp. 1943–1954, May 2013.

[21] M. Hagiwara, I. Hasegawa, and H. Akagi, "Start-up and low-speed operation of an electric motor driven by a modular multilevel cascade inverter," *IEEE Trans. Ind. Appl.*, vol. 49, no. 4, pp. 1556–1565, Jul./Aug. 2013.

[22] Y. Okazaki, M. Hagiwara, and H. Akagi, "A speed-sensorless start-up method of an induction motor driven by a modular multilevel cascade inverter (MMCI-DSCC)," *IEEE Trans. Ind. Appl.*, vol. 50, no. 4, pp. 2671–2680, Jul./Aug. 2014.

[23] J. Jung, H. Lee, and S.-K. Sul, "Control strategy for improved dynamic performance of variable-speed drives with modular multilevel converter," *IEEE J. Emerging Sel. Topics Power Electron.*, vol. 3, no. 2, pp. 371–380, Jun. 2015.

[24] B. Li *et al.*, "An improved circulating current injection method for modular multilevel converters in variable-speed drives," *IEEE Trans. Ind. Electron.*, vol. 63, no. 11, pp. 7215–7225, Nov. 2016.

[25] A. Antonopoulos, L. Ängquist, L. Harnefors, and H. P. Nee, "Optimal selection of the average capacitor voltage for variable-speed drives with modular multilevel converters," *IEEE Trans. Power Electron.*, vol. 30, no. 1, pp. 227–234, Jan. 2015.

[26] B. Tai, C. Gao, X. Liu, and Z. Chen, "A novel flexible capacitor voltage control strategy for variable-speed drives with modular multilevel converters," *IEEE Trans. Power Electron.*, vol. 32, no. 1, pp. 128–141, Jan. 2017.

[27] R. Yang, B. Li, G. Wang, C. Cecati, S. Zhou, D. G. Xu, and W. Yu, "Asymmetric mode control of MMC to suppress capacitor voltage ripples in low frequency low voltage condition," *IEEE Trans. Power Electron.*, vol. 32, no. 6, pp. 4219–4230, Jun. 2017.

[28] G. P. Adam, S. J. Finney, A. M. Massoud, and B. W. Williams, "Capacitor balance issues of the diode-clamped multilevel inverter operated in a quasi two-state mode," in *IEEE Trans. Ind. Electron*, vol. 55, no. 8, pp. 3088–3099, Aug. 2008.

[29] A. Mertens and J. Kucka, "Quasi two-level PWM operation of an MMC phase leg with reduced module capacitance," *IEEE Trans. Power Electron.*, vol. 31, no. 10, pp. 6765–6769, Oct. 2016.

[30] S. Du, B. Wu, K. Tian, N. R. Zargari, and Z. Cheng, "An active cross-connected modular multilevel converter (AC-MMC) for a medium-voltage motor drive," *IEEE Trans. Ind. Electron*, vol. 63, no. 8, pp. 4707–4717, Aug. 2016.

[31] S. Du, B. Wu, N. Zargari, and Z. Cheng, "A flying-capacitor modular multilevel converter (FC-MMC) for medium-voltage motor drive," *IEEE Trans. Power Electron.*, vol. 32, no. 3, pp. 2081–2089, Mar. 2017.

[32] L. He, K. Zhang, J. Xiong, S. Fan, and Y. Xue, "Low-frequency ripple suppression for medium-voltage drives using modular multilevel converter with full-bridge submodules," *IEEE J. Emerging Sel. Topics Power Electron.*, vol. 4, no. 2, pp. 657–667, Jun. 2016.

[33] L. Baruschka, D. Karwatzki, M. von Hofen, and A. Mertens, "Low-speed drive operation of the modular multilevel converter Hexverter down to zero frequency," in *Proc. 2014 IEEE Energy Convers. Congr. Expo.*, Pittsburgh, PA, USA, 2014, pp. 5407–5414.

[34] B. Li, S. Zhou, D. Xu, S. J. Finney, and B. W. Williams, "A hybrid modular multilevel converter for medium-voltage variable-speed motor drives," *IEEE Trans. Power Electron.*, vol. 32, no. 6, pp. 4619–4630, Jun. 2017.

[35] B. Li, Y. Zhang, G. Wang, W. Sun, D. Xu, and W. Wang, "A modified modular multilevel converter with reduced capacitor voltage fluctuation," *IEEE Trans. Ind. Electron.*, vol. 62, no. 10, pp. 6108–6119, Oct. 2015.

[36] A. Somani, R. Gupta, K. Mohapatra, and N. Mohan, "On the causes of circulating currents in PWM drives with open-end winding ac machines," *IEEE Trans. Ind. Electron.*, vol. 60, no. 9, pp. 3670–3678, Sep. 2013.

[37] M. R. Baiju, K. K. Mohapatra, R. S. Kanchan, and K. Gopakumar, "A dual two-level inverter scheme with common mode voltage elimination for an induction motor drive," *IEEE Trans. Power Electron.*, vol. 19, no. 3, pp. 794–805, May 2004.

[38] N. Bodo, M. Jones, and E. Levi, "A space vector PWM with common mode elimination for open-end winding five-phase drives with a single dc supply," *IEEE Trans. Ind. Electron.*, vol. 61, no. 5, pp. 2197–2207, May 2014.
[39] P. Rajeevan, K. Sivakumar, K. Gopakumar, C. Patel, and H. Abu-Rub, "A nine-level inverter topology for medium-voltage induction motor drive with open-end stator winding," *IEEE Trans. Ind. Electron.*, vol. 60, no. 9, pp. 3627–3636, Sep. 2013.
[40] M. Darijevic, M. Jones, and E. Levi, "An open-end winding four-level five-phase drive," *IEEE Trans. Ind. Electron.*, vol. 63, no. 1, pp. 538–549, Jan. 2016.
[41] H. Stemmler and P. Guggenbach, "Configurations of high-power voltage source inverter drives," in *Proc. 5th Eur. Conf. Power Electron. Appl.*, 1993, vol. 5, pp. 7–14.
[42] K. Corzine, M. Wielebski, F. Peng, and J. Wang, "Control of cascaded multilevel inverters," *IEEE Trans. Power Electron.*, vol. 19, no. 3, pp. 732–738, May 2004.
[43] V. Somasekhar, K. Gopakumar, M. R. Baiju, K. Mohapatra, and L. Umanand, "A multilevel inverter system for an induction motor with open-end windings," *IEEE Trans. Ind. Electron.*, vol. 52, no. 3, pp. 824–836, Jun. 2005.
[44] R. S. Kanchan, P. N. Tekwani, and K. Gopakumar, "Three-level inverter scheme with common mode voltage elimination and dc link capacitor voltage balancing for an open-end winding induction motor drive," *IEEE Trans. Power Electron.*, vol. 21, no. 6, pp. 1676–1683, Nov. 2006.
[45] G. Mondal, K. Gopakumar, P. N. Tekwani, and E. Levi, "A reduced-switch count five-level inverter with common-mode voltage elimination for an open-end winding induction motor drive," *IEEE Trans. Ind. Electron.*, vol. 54, no. 4, pp. 2344–2351, Aug. 2007.
[46] A. Edpuganti and A. K. Rathore, "Optimal pulse-width modulation for common-mode voltage elimination scheme of medium-voltage modular multilevel converter-fed open-end stator winding induction motor drives," *IEEE Trans. Ind. Electron.*, vol. 64, no. 1, pp. 848–856, Jan. 2017.
[47] K. Ilves, A. Antonopoulos, S. Norrga, and H.-P. Nee, "Steady-state analysis of interaction between harmonic components of arm and line quantities of modular multilevel converters," *IEEE Trans. Power Electron.*, vol. 27, no. 1, pp. 57–68, Jan. 2012.
[48] Z. Li, P. Wang, Z. Chu, H. Zhu, Y. Luo, and Y. Li, "An inner current suppressing method for modular multilevel converters," *IEEE Trans. Power Electron.*, vol. 28, no. 11, pp. 4873–4879, Nov. 2013.
[49] Q. Tu, Z. Xu, and L. Xu, "Reduced switching-frequency modulation and circulating current suppression for modular multilevel PWM converters," *IEEE Trans. Power Del.*, vol. 26, no. 3, pp. 2009–2017, Jul. 2011.
[50] R. W. A. A. De Doncker, D. M. Divan, and M. H. Kheraluwala, "A three-phase soft-switched high-power-density DC/DC converter for high-power applications," *IEEE Trans. Ind. Appl.*, vol. 27, no. 1, pp. 63–73, Jan./Feb. 1991.
[51] S. Inoue and H. Akagi, "A bidirectional isolated DC–DC converter as a core circuit of the next-generation medium-voltage power conversion system," *IEEE Trans. Power Electron.*, vol. 22, no. 2, pp. 535–542, Mar. 2007.
[52] M. H. Kheraluwala and R. W. Gascoigne, "Performance characterization of a high-power dual active bridge dc-to-dc converter," *IEEE Trans. Ind. Appl.*, vol. 28, no. 6, pp. 1294–1301, Nov./Dec. 1992.
[53] F. Z. Peng, H. Li, G.-J. Su, and J. S. Lawler, "A new ZVS bidirectional dc–dc converter for fuel cell and battery application," *IEEE Trans. Power Electron.*, vol. 19, no. 1, pp. 54–65, Jan. 2004.
[54] E. R. Ronan, S. D. Sudhoff, S. F. Glover, and D. L. Galloway, "A power electronic-based distribution transformer," *IEEE Trans. Power Del.*, vol. 17, no. 2, pp. 537–543, Apr. 2000.
[55] *ABB HiPak 5SNA 1200G450350*, 2016. [Online]. Available: https://library.e.abb.com/public/afe3c7e548fe45ff8e4506203449f363/5SNA%201200G450350_5SYA%201415-04%2003-2016.pdf
[56] *ABB HiPak 5SNA 0650J450300*, 2016. [Online]. Available: https://library.e.abb.com/public/3292e84562f947b1aea83bdb9c408df8/5SNA%200650J450300_5SYA%201598-05%2005-2016.pdf
[57] (2009). *EPOCS Product Brief 2009. Power Capacitors*, 2016. [Online]. Available: http://www.rollay.com.cn/ImgUpload/Articleimage/201007091740522.pdf
[58] ETHZ MegaCube Project, 2013. [Online]. Available: https://www.pes.ee.ethz.ch/uploads/tx_ethpublications/01_MegaCube_Trafo_Digest_APEC2013.pdf
[59] M. Leibl, G. Ortiz, and J. W. Kolar, "Design and experimental analysis of a medium-frequency transformer for solid-state transformer applications," *IEEE J. Emerging Sel. Topics Power Electron.*, vol. 5, no. 1, pp. 110–123, Mar. 2017.
[60] G. Ortiz, M. Leibl, J. W. Kolar, and O. Apeldoorn, "Medium frequency transformers for solid-state-transformer applications—Design and experimental verification," in *Proc. 2013 IEEE 10th Int. Conf. Power Electron. Drive Syst.*, Kitakyushu, Japan, 2013, pp. 1285–1290.

Mohamed S. Diab received the B.Sc. (First Class Hons.) and M.Sc. degrees in electrical engineering from Alexandria University, Alexandria, Egypt, in 2012, and 2015, respectively. He is currently working toward the Ph.D. degree in electrical engineering at the University of Strathclyde, Glasgow, U.K.

He was in the Department of Electrical Engineering, Alexandria University, where he was appointed as a Demonstrator in 2012 and as an Assistant Lecturer in 2015. He was with Spiretronic LLC, Houston, TX, USA, as a Research Engineer, from 2013 to 2015. His main research interests include medium-voltage applications, high-power electronic converters, renewable energy conversion systems, grid integration of distributed generators, and electric drives.

Ahmed M. Massoud (SM'11) received the B.Sc. (First Class Hons.) and M.Sc. degrees in electrical engineering from Alexandria University, Alexandria, Egypt, in 1997 and 2000, respectively, and the Ph.D. degree in electrical engineering from Heriot-Watt University, Edinburgh, U.K., in 2004.

From 2005 to 2008, he was a Research Fellow with Strathclyde University, Glasgow, U.K. From 2008 to 2009, he was a Research Fellow with Texas A&M at Qatar, Doha, Qatar. From 2009 to 2012, he was an Assistant Professor in the Department of Electrical Engineering, College of Engineering, Qatar University, Doha, where he is currently an Associate Professor in the same department. His research interests include power electronics, energy conversion, renewable energy, and power quality.

Shehab Ahmed (SM'12) received the B.Sc. degree from Alexandria University, Alexandria, Egypt, in 1999, and the M.Sc. and Ph.D. degrees from the Department of Electrical and Computer Engineering, Texas A&M University, College Station, TX, USA, in 2000 and 2007, respectively, all in electrical engineering.

He was with Schlumberger Technology Corporation, Houston, TX, USA, from 2001 to 2007, where he was involved in downhole mechatronic systems. He is currently an Associate Professor with Texas A&M University at Qatar, Doha, Qatar. His research interests include mechatronics, solid-state power conversion, electric machines, and drives.

Barry W. Williams received the M.Eng.Sc. degree from the University of Adelaide, Adelaide, S.A., Australia, in 1978, and the Ph.D. degree from Cambridge University, Cambridge, U.K., in 1980, both in electrical engineering.

After seven years as a Lecturer with Imperial College, University of London, London, U.K., he was appointed to a Chair of the Electrical Engineering, Heriot-Watt University, Edinburgh, U.K., in 1986. He is currently a Professor with the University of Strathclyde, Glasgow, U.K. His teaching covers power electronics (in which he has a free internet text) and drive systems. His research interests include power semiconductor modeling and protection, converter topologies, soft-switching techniques, and application of ASICs and microprocessors to industrial electronics.